



Inversion of the Lyman α forest: three-dimensional investigation of the intergalactic medium

C. Pichon, J. L. Vergely, E. Rollinde, S. Colombi

► To cite this version:

C. Pichon, J. L. Vergely, E. Rollinde, S. Colombi. Inversion of the Lyman α forest: three-dimensional investigation of the intergalactic medium. Monthly Notices of the Royal Astronomical Society, 2001, 326, pp.597-620. 10.1046/j.1365-8711.2001.04595.x . insu-04054633

HAL Id: insu-04054633

<https://insu.hal.science/insu-04054633>

Submitted on 1 Apr 2023

HAL is a multi-disciplinary open access archive for the deposit and dissemination of scientific research documents, whether they are published or not. The documents may come from teaching and research institutions in France or abroad, or from public or private research centers.

L'archive ouverte pluridisciplinaire **HAL**, est destinée au dépôt et à la diffusion de documents scientifiques de niveau recherche, publiés ou non, émanant des établissements d'enseignement et de recherche français ou étrangers, des laboratoires publics ou privés.

Inversion of the Lyman α forest: three-dimensional investigation of the intergalactic medium

C. Pichon,^{1,2,3★} J. L. Vergely,^{1,4} E. Rollinde,² S. Colombi^{2,3} and P. Petitjean^{2,5}

¹*Observatoire de Strasbourg, 11 rue de l'Université, 67000 Strasbourg, France*

²*Institut d'Astrophysique de Paris, 98 bis boulevard d'Arago, 75014 Paris, France*

³*Numerical Investigations in Cosmology (NIC), CNRS, France*

⁴*Institute of Astronomy, Madingley Road, Cambridge CB3 0HA*

⁵*UA CNRS 173 – DAEC, Observatoire de Paris-Meudon, F-92195 Meudon Cedex, France*

Accepted 2001 April 17. Received 2001 March 22; in original form 2000 August 7

ABSTRACT

We discuss the implementation of Bayesian inversion methods in order to recover the properties of the intergalactic medium from observations of the neutral hydrogen Lyman α absorptions observed in the spectra of high-redshift quasars (the so-called Lyman α forest). We use two complementary schemes: (i) a constrained Gaussian random field linear approach, and (ii) a more general non-linear explicit Bayesian deconvolution method, which offers in particular the possibility to constrain the parameters of the equation of state for the gas.

The interpolation ability of the first approach is shown to be equivalent to the second one in the limit of negligible measurement errors, low-resolution spectra and null mean prior.

While relying on prior assumption for the two-point correlation functions, we show how to recover, at least qualitatively, the three-dimensional topology of the large-scale structures in redshift space by inverting a suitable network of adjacent, low-resolution lines of sight. The methods are tested on regular bundles of lines of sight using N -body simulations specially designed to tackle this problem.

We also discuss the inversion of single lines of sight observed at high spectral resolution. Our preliminary investigations suggest that the explicit Bayesian method can be used to derive quantitative information on the physical state of the gas when the effects of redshift distortion are negligible. The information in the spectra remains degenerate with respect to two parameters (the temperature scale factor and the polytropic index) describing the equation of state of the gas.

Redshift distortion is considered by simultaneous constrained reconstruction of the velocity and the density field in real space, while assuming statistical correlation between the two fields. The method seems to work well in the strong prior régime where peculiar velocities are assumed to be the most likely realization in the density field. Finally, we investigate the effect of line-of-sight separation and number of lines of sight. Our analyses suggest that multiple low-resolution lines of sight could be used to improve the most likely velocity reconstruction on a high-resolution line of sight.

Key words: methods: data analysis – methods: N -body simulations – methods: statistical – intergalactic medium – quasars: absorption lines – dark matter.

1 INTRODUCTION

It has been realized recently that the cosmological mass density of the baryons located in the intergalactic medium (IGM) at high redshift is similar to the total cosmological mass density of baryons predicted by primordial nucleosynthesis theories (Meiksin & Madau 1993; Petitjean

★E-mail: pichon@astro.u-strasbg.fr

et al. 1993; Press & Rybicki 1993; Rauch et al. 1997; Valageas, Schaeffer & Silk 1999). Therefore there is probably a close interplay between galaxy formation and IGM evolution. The IGM acts as the baryonic reservoir for galaxy formation, while star formation activity in forming galaxies should influence the physical state of the IGM through metal enrichment and emission of ionizing radiation. Hence it would be of primary interest to be able to correlate the spatial distribution of intergalactic gas with that of galaxies.

Neutral hydrogen in the IGM is revealed by the numerous absorption lines seen in QSO spectra (the so-called Lyman α forest). The physics of the gas is remarkably simple: its thermal state is governed by photoionization heating and adiabatic cooling (e.g. Hui & Gnedin 1997; Weinberg 1999), and its dynamics results from the effects of gravity on large scales and pressure smoothing on small scales (Reisenegger & Miralda-Escudé 1995; Bi & Davidsen 1997; Hui, Gnedin & Zhang 1997). Dark matter and baryons trace each other quite well, and the Lyman α forest is due to mildly overdense fluctuations in a pervasive medium with density contrasts of the order of 1 to 10. The gas should be distributed along filaments and/or sheets of significant extension.

This is supported by observations of multiple lines of sight (LOSs) showing that the gaseous complexes producing the Lyman α forest have large sizes. Indeed, in the spectra of multiple images of lensed quasars with separations of the order of a few arcsec (Smette et al. 1995; Impey et al. 1996), the Lyman α forests appear nearly identical, implying that the absorbing objects have sizes $> 50 h_{75}^{-1}$ kpc.¹ Pairs with separation up to $500 h_{75}^{-1}$ kpc show an excess of absorptions common to both LOSs compared to what is expected for an uncorrelated distribution of absorption lines (Dinshaw et al. 1995; Crofts & Fang 1998; D’Odorico et al. 1998; Petitjean et al. 1998). This suggests rather large dimensions or better coherence length and a non-spherical geometry of the absorbing structures (Rauch & Haehnelt 1995).

Recent N -body simulations have provided a consistent theoretical framework for the description of the IGM (Cen et al. 1994; Petitjean, Mücke & Kates 1995; Zhang, Anninos & Norman 1995; Hernquist et al. 1996; Miralda-Escudé et al. 1996; Mücke et al. 1996; Bond & Wadsley 1998). The simulations are very successful at reproducing the main characteristics of the Lyman α forest: the column density distribution, the Doppler parameter distribution, the flux decrement distribution and the redshift evolution of absorption lines. It has become clear that the Lyman α forest is a powerful tool to investigate key cosmological issues such as the re-ionization of the Universe (Abel & Haehnelt 1999; Schaye et al. 1999; Ricotti, Gnedin & Shull 2000), the density fluctuation power spectrum (Croft et al. 1998; Gnedin & Hui 1998; Hui 1999; Nusser & Haehnelt 1999a), the geometry of the Universe (Hui, Stebbins & Burles 1999) or cosmological parameters (Weinberg et al. 1999).

Applications to real data have led to interesting constraints on the fluctuation power spectrum (Croft et al. 1999; Nusser & Haehnelt 1999b), cosmological parameters (Weinberg et al. 1999; Theuns, Schaye & Haehnelt 2000) or the physical characteristics of the gas (Schaye et al. 1999). However, these studies are presently limited by the amount of information available, and show that it is important to increase current LOS data sets.

Two approaches can be considered: (i) increasing the number of LOSs observed at intermediate and high spectral resolution in order to improve the precision of the above measurements; large redshift surveys in progress or in preparation such as the Sloan Digital Sky Survey (SDSS; e.g. Szalay 2000) the Two degree Field (2dF; e.g. Folkes et al. 1999) or the VIRMOS redshift survey (e.g. Le Fèvre et al. 1998) should dramatically increase the number of low spectral resolution QSO spectra available for analysis; (ii) using groups of QSOs to constrain the three-dimensional (3D) distribution of the gas and to study redshift-space distortion effects, taking into account peculiar velocities in the reconstruction; the ultimate goal would be to increase the density of LOSs so that the reconstructed 3D spatial distribution of the gas can be correlated with galaxies observed in the same field; the deep imaging surveys planned with MEGACAM (e.g. Boulade et al. 1998) at the Canada-France-Hawaii Telescope and follow-up spectroscopy should provide data for such projects.

It is thus of first importance to prepare the tools needed for the interpretation of the wealth of data that will be provided by the planned surveys. Nusser & Haehnelt (1999a) have described a method for the recovery of the real-space density distribution along one LOS. Using an analytical model of the IGM, they propose a direct inversion of the Lyman α forest seen in the QSO spectra using an iterative scheme based on Lucy’s deconvolution method (Lucy 1974). This method yields fields for the density in contrast to Voigt profile decomposition.

Here we show that these techniques can be generalized to multiple LOSs to reconstruct the 3D density field (see Vergely et al. 2001 for a similar application to the 3D mapping of the local interstellar medium). This should help for characterizing the structures (filaments, sheets...), determining physical properties of the gas (temperature, peculiar velocity) and discussing the cosmological evolution of the IGM.

This paper is organized as follows. In Section 2 we present basic equations describing the relationship between absorption along LOSs and properties of the IGM. Section 3 is concerned with sketching the basis for the inversion technique; two methods are described, a Bayesian regularized inverse method and a constrained random Gaussian field reconstruction, which can actually be seen as a particular case of the first method. Section 4 describes two N -body simulations from which we construct simulated data. Section 5 discusses the use of inversion techniques implemented here (i) to recover the 3D spatial distribution of the IGM from Lyman α forest absorption lines on large scales while neglecting thermal broadening, (ii) to address the issue of thermal broadening on small scales, and (iii) to take into account peculiar velocities and correction for the induced redshift distortions.

2 THE LYMAN- α OPTICAL DEPTH ALONG A LINE OF SIGHT

The optical depth, $\tau_\ell(w)$, along the LOS ℓ , at projected position $\mathbf{x}_{\perp,\ell} \equiv (y_\ell, z_\ell)$ on the sky, and in velocity space, w , is related to neutral

¹where h_{75} is the Hubble constant expressed in units of $75 \text{ km s}^{-1} \text{ Mpc}^{-1}$.

hydrogen density, n_{HI} , by

$$\tau_\ell(w) = \frac{c\sigma_0}{H(\bar{z})\sqrt{\pi}} \int \int \left[\int_{-\infty}^{+\infty} \frac{n_{\text{HI}}(x, \mathbf{x}_\perp)}{b(x, \mathbf{x}_\perp)} \exp \left\{ -\frac{[w - x - v_p(x, \mathbf{x}_\perp)]^2}{b(x, \mathbf{x}_\perp)^2} \right\} dx \right] \delta_D(\mathbf{x}_\perp - \mathbf{x}_{\perp, \ell}) d^2 \mathbf{x}_\perp, \quad \ell = 1 \dots L, \quad (1)$$

where σ_0 is the effective cross-section for resonant line scattering, $H(\bar{z})$ is the Hubble constant at mean redshift \bar{z} , and $v_p(x)$ is the projection of the peculiar velocity along the LOS. The double sum over \mathbf{x}_\perp corresponds to the integration in the directions perpendicular to the LOSs. δ_D is the 2D Dirac distribution. The Doppler parameter $b(x)$ is considered a function of the local temperature of the IGM at point $\mathbf{x} \equiv (x, \mathbf{x}_\perp)$ where x is the real-space coordinate expressed in $\text{km}^{-1} [= rH(\bar{z})]$.

This work is concerned with assessing the inversion of equation (1) with the aim of constraining the 3D fields, $n_{\text{HI}}(x, \mathbf{x}_\perp)$, $b(x, \mathbf{x}_\perp)$ and $v_p(x, \mathbf{x}_\perp)$, from the knowledge of a bundle of LOSs, $\ell = 1 \dots L$.

2.1 The model

To relate the gas density, the dark matter (DM) density and the temperature, we follow the prescriptions of Hui & Gnedin (1997). We refer to this paper for a detailed derivation of the relations given below. We assume that baryons trace DM potential (Bi & Davidsen 1997) and are in ionization equilibrium. Therefore

$$n_{\text{HI}} \propto \rho_{\text{DM}}^2 T^{-0.7}, \quad (2)$$

where n_{HI} is the neutral hydrogen particle density, and ρ_{DM} the dark matter density.

Considering that shock heating is unimportant for the thermal budget of the intergalactic gas (Hui & Gendin 1997), an effective equation of state describes the physical state of the gas,

$$T(x) = \bar{T} \left[\frac{\rho_{\text{DM}}(x)}{\bar{\rho}_{\text{DM}}} \right]^{2\beta}. \quad (3)$$

The parameter β is in the interval $0 < \beta < 0.31$ (this upper bound corresponds to the asymptotic value at $z = 0$ far from re-ionization). Therefore

$$n_{\text{HI}}(x) = \bar{n}_{\text{HI}} \left[\frac{\rho_{\text{DM}}(x)}{\bar{\rho}_{\text{DM}}} \right]^\alpha \quad \text{with a scaling} \quad \alpha = 2 - 1.4\beta. \quad (4)$$

If there is no turbulence, then the Doppler parameter $b(x)$ at each position is due to thermal broadening only,

$$b(x) = 13 \text{ km s}^{-1} \sqrt{\frac{\bar{T}}{10^4 \text{ K}}} \left[\frac{\rho_{\text{DM}}(x)}{\bar{\rho}_{\text{DM}}} \right]^\beta, \quad (5)$$

and equation (1) becomes

$$\tau_\ell(w) = A(\bar{z}) c_1 \int \int \left[\frac{\rho_{\text{DM}}(x, \mathbf{x}_\perp)}{\bar{\rho}_{\text{DM}}} \right]^{\alpha-\beta} \exp \left\{ -c_2 \frac{[w - x - v_p(x, \mathbf{x}_\perp)]^2}{[\rho_{\text{DM}}(x, \mathbf{x}_\perp)/\bar{\rho}_{\text{DM}}]^{2\beta}} \right\} dx \delta_D(\mathbf{x}_\perp - \mathbf{x}_{\perp, \ell}) d^2 \mathbf{x}_\perp. \quad (6)$$

The parameters c_1 and c_2 depend on the characteristic temperature of the IGM:

$$c_1 = \left(13 \sqrt{\pi} \sqrt{\frac{\bar{T}}{10^4}} \right)^{-1}, \quad c_2 = \left(13^2 \frac{\bar{T}}{10^4} \right)^{-1} \quad \text{and} \quad A(\bar{z}) = \bar{n}_{\text{HI}} \frac{c\sigma_0}{H(\bar{z})} \propto \frac{\bar{T}^{-0.7}}{J}, \quad (7)$$

where J is the ionizing flux, assumed to be uniform. Here the temperatures are given in Kelvin. The value of $A(\bar{z})$ is fixed by matching the observed average optical depth (≈ 0.2 at $\bar{z} = 2$).

2.2 The régimes of interest for the reconstruction

Several régimes will be considered in Section 5 when performing the inversion.

(i) *Small scales or high resolution* ($\ell \lesssim 0.1 \text{ Mpc}$) : In this régime, and although it might not necessarily be a good approximation (e.g. Hui et al. 1997), we simply assume that redshift distortion is negligible ($v_p = 0$ in equation 6), and reconstruct the density field in redshift space while constraining the equation of state.

(ii) *Large scales or low resolution* ($\ell \gtrsim 1 \text{ Mpc}$) : In this régime, applicable to low-resolution spectra, thermal broadening can be neglected and equation (1) simply becomes

$$\tau_\ell(w) = A(\bar{z}) \int \int \left[\frac{\rho_{\text{DM}}\{w - v_p[x(w, \mathbf{x}_\perp)], \mathbf{x}_\perp\}}{\bar{\rho}_{\text{DM}}} \right]^\alpha \delta_D(\mathbf{x}_\perp - \mathbf{x}_{\perp, \ell}) d^2 \mathbf{x}_\perp, \quad \text{for } \ell = 1 \dots L, \quad (8)$$

where $x(w, \mathbf{x}_\perp)$ is defined implicitly by the equation $x = w - v_p(x, \mathbf{x}_\perp)$. Our efforts in this régime will focus on 3D reconstruction of the density in redshift space, i.e., with $v_p = 0$ in equation (8) and known equation of state for the gas. In principle, redshift distortion should not be neglected, but this does not change significantly the topology of large-scale structures, at least at weakly non-linear scales, thus making such simplified analysis still relevant.

(iii) *Intermediate scales or intermediate resolution* ($0.1 \lesssim \ell \lesssim 1$ Mpc) : Redshift distortion will not be neglected anymore, and equation (6) will be used to determine simultaneously the density and velocity fields, assuming that the effective equation of state is known.

Note that we neglect here the statistical scatter away from equation (3) and in particular the departure from a unique power law for larger overdensities.

3 DECONVOLUTION OF THE IGM

The basic idea is to interpolate between adjacent LOSs the fields which are measured along the LOSs. This first requires assumptions on the nature of the fields. In fact, strictly speaking, our ability to say anything away from the LOSs could be questioned, since to the best of our unbiased knowledge, space between the LOSs could well be empty. Moreover, the inversion of equation (1) is obviously not unique, and additional assumptions must be made in order to reduce the parameter space. For example, the Doppler parameter and/or the peculiar velocity fields are taken to be described by a simple function of the sought density field, $n_{\text{H I}}$. Indeed, dynamical considerations supported by numerical simulations suggest there exists a statistical relationship between overdensities and the corresponding projected velocity field, while temperature and density are also statistically related by an equation of state.

This paper addresses these issues via two techniques.

(i) A general, explicit Bayesian deconvolution method (Section 3.1), capable of dealing with fields and priors such as a given equation of state. This method should allow one to deconvolve thermal broadening non-linearly, while accounting for peculiar velocities, and therefore to reconstruct the density/velocity field along a LOS and constrain the equation of state of the gas. With several LOSs, it should simultaneously be possible to obtain the 3D density field.

(ii) A constrained Gaussian random field linear approach (Section 3.2), which relates the peculiar velocities projected along the LOS to the 3D density field, or directly the 3D density field to the LOS density in redshift space. It requires prior knowledge of the logarithm of density in redshift space along each LOS, but can be used after applying method (i) to each LOS.

In fact, method (i) is very general and can be applied in many ways, which differ mainly in the priors taken for the statistical properties of the density and velocity fields. Method (ii) corresponds to a given choice of strategy for the 3D density/velocity reconstruction step: like Wiener filtering, it is a particular case of method (i) (Section 3.3).

3.1 A non-parametric explicit Bayesian regularized inverse method

We aim to invert equation (1), i.e., reconstruct the density field $n_{\text{H I}}$ and the velocity field $v_p(x, \mathbf{x}_\perp)$. To that end, we take a *model*, g , such as equations (3)–(5), which basically relate the Doppler parameter b and the gas density $n_{\text{H I}}$ to the dark matter density, ρ_{DM} , and obtain equation (6). In this equation, there are a certain number of *parameters* to be determined, which can be continuous fields such as the DM density or the velocity field, or discrete parameters such as α and β . This set of parameters can be formally described as a vector, \mathbf{M} . The goal here is to determine \mathbf{M} by fitting the data, \mathbf{D} , i.e., the absorption spectra along the N LOSs.

Since the problem is underdetermined, we use a Bayesian technique described in Tarantola & Valette (1982a; see also, e.g., Craig & Brown 1986 and Pichon & Thiébaud 1998). In order to achieve regularization, this method requires a prior guess for the parameters, or in statistical terms, their probability distribution function, $f_{\text{prior}}(\mathbf{M})$.

Using Baye's theorem, the conditional probability density $f_{\text{post}}(\mathbf{M}|\mathbf{D})$ for the realization \mathbf{M} given the observed data \mathbf{D} then writes:

$$f_{\text{post}}(\mathbf{M}|\mathbf{D}) = \mathcal{L}(\mathbf{D}|\mathbf{M})f_{\text{prior}}(\mathbf{M}), \quad (9)$$

where \mathcal{L} is the likelihood function of the data given the model.

If we assume that both functions \mathcal{L} and f_{prior} are Gaussian, we can write

$$f_{\text{post}}(\mathbf{M}|\mathbf{D}) = \mathcal{A} \exp \left\{ -\frac{1}{2} [\mathbf{D} - g(\mathbf{M})]^\perp \cdot \mathbf{C}_d^{-1} \cdot [\mathbf{D} - g(\mathbf{M})] - \frac{1}{2} (\mathbf{M} - \mathbf{M}_0)^\perp \cdot \mathbf{C}_0^{-1} \cdot (\mathbf{M} - \mathbf{M}_0) \right\}, \quad (10)$$

with \mathbf{C}_d and \mathbf{C}_0 being respectively the covariance 'matrix'² of the observed noise and of the prior guess for the parameters, \mathbf{M}_0 . \mathcal{A} is a normalization constant. The superscript, \perp , stands for transposition. The first argument of the exponential in equation (10) corresponds to the likelihood of the data, given the model and the parameters,³ while the last corresponds to the likelihood of the parameters, given the prior \mathbf{M}_0 . Note that the assumption of a Gaussian field for f_{prior} could be lifted, in particular to account for the presence of contrasted filaments (i.e., we could introduce three-point correlation functions, or higher order statistics to account for the fact that, say, the prior likelihood of aligned

²Formally defined on continuous + discrete fields, as is the vector \mathbf{M} .

³Note that the model g taken here would correspond to equation (6) instead of equations (3)–(5) as said earlier.

overdensities is higher). A possible method for maximizing the posterior probability given in equation (10) is sketched in Appendix A. In a nutshell, the minimum, $\langle \mathbf{M} \rangle$, of the argument of the exponential in equation (10) is shown by a simple variational argument (Tarantola & Valette 1982a,b) to obey the implicit equation

$$\langle \mathbf{M} \rangle = \mathbf{M}_0 + \mathbf{C}_0 \cdot \mathbf{G}^\perp \cdot (\mathbf{C}_d + \mathbf{G} \cdot \mathbf{C}_0 \cdot \mathbf{G}^\perp)^{-1} \cdot (\mathbf{D} + \mathbf{G} \cdot (\langle \mathbf{M} \rangle - \mathbf{M}_0) - g(\langle \mathbf{M} \rangle)), \quad (11)$$

where \mathbf{G} is the matrix (or, more rigorously, the functional operator) of partial derivatives of the model $g(\mathbf{M})$ with respect to the parameters. Note that, under the assumption of Gaussianity, the extremum $\langle \mathbf{M} \rangle$ is at the same time the most likely constrained value of the parameters vector and its mean value. The posterior covariances of the parameters, \mathbf{C}_M , can be computed from equation (A6).

The method can in principle be iterated, taking in equation (11) $\mathbf{M}_0 = \mathbf{M}$ and $\mathbf{C}_0 = \mathbf{C}_M$ to compute a new value of \mathbf{M} until possible convergence. However, in this paper we did not test this procedure.

We might then wonder how the choice of the prior for the parameters, \mathbf{M}_0 and their covariance matrix, \mathbf{C}_0 , affect the final result, $\langle \mathbf{M} \rangle$. We will show in Section 3.3 that for null prior, $\mathbf{M}_0 = 0$, the method proposed here is equivalent to Wiener filtering if the model is linear [$g(\mathbf{M}) = \mathbf{G} \cdot \mathbf{M}$]. However, we may include more prior information when possible. For instance, if in the field of interest, redshifts of galaxies and clusters, gravitational lensing or SZ data, etc., is available, we may explicitly incorporate these additional constraints in the prior \mathbf{M}_0 instead of extending the data set, \mathbf{D} . More realistic expressions accounting for the statistical scatter around equation (3) and a possible slope break are also possible. Additional information about our prejudice on the evolution of large-scale structures can also be incorporated in the description of the prior probability distribution function to account for, say, dynamically induced non-Gaussianity.

3.2 Constrained mean field reconstruction

In principle, the explicit Bayesian method described above can be applied to the data to reconstruct along each LOS the density field in redshift space while constraining the equation of state, as illustrated in Section 5.3. When dealing with the large-scale régime of Section 2.2, equation (8) applies, and the density contrast, defined by

$$\delta(x) \equiv \log(\rho_{\text{DM}}/\bar{\rho}_{\text{DM}}) \approx (\rho_{\text{DM}} - \bar{\rho}_{\text{DM}})/\bar{\rho}_{\text{DM}}, \quad (12)$$

reads, along each LOS and in redshift space ($x = w$),

$$\delta_\ell(x, \mathbf{x}_\perp) = \frac{1}{\alpha} \log \left[\frac{\tau_\ell(x)}{A(\bar{z})} \right]. \quad (13)$$

This section focuses on recovering the 3D density field in redshift space or in real space, the latter case requiring treatment of peculiar velocities. To achieve that, we use a constrained mean field method (e.g. Hoffman & Ribak 1992). Broadly speaking, such a method assumes that part of a model (here the density in redshift space along the LOSs) is fixed by the observations. It then provides the relation between these ‘data’ and the most likely value of the remaining part of the parameters (here the density between the LOSs and the full 3D velocity field). This method requires some assumptions on the statistical properties of the searched fields. The idea is to consider large enough scales so that non-linear effects have not driven the system dynamically too far away from its initial conditions, which we assume to be Gaussian-distributed.⁴ The theory of constrained random Gaussian fields is well known (e.g. Rice 1944, 1945; Longuet-Higgins 1957; Adler 1981; Bardeen et al. 1986, and references therein), and application to our problem is detailed in Appendix B.

We assume that the constraints are distributed along a bundle of L LOSs, i.e., that the density contrast (defined above in equation 12) takes the values $[\delta_\ell(x)]_{\ell=1\dots L}$ along the LOSs. Then, using linear perturbation theory and the Gaussian nature of underlying fields, we can write the probability distribution function of the 3D velocity or density field in redshift space in terms of these constraints and of the 3D power spectrum of the density field, $P_{3D}(\mathbf{k})$. A prior is thus required for $P_{3D}(\mathbf{k})$, but an iterative procedure can in principle be implemented, using the $P_{3D}(\mathbf{k})$ measured in the reconstructed data after redshift distortion deconvolution as a new prior.

We demonstrate that the most likely velocity $\langle v_p \rangle_\ell$ along the LOS ℓ is given by the linear relationship (equation B14)

$$\langle v_p \rangle_\ell(x) = \sum_{\ell'} \int K_{\ell\ell'}(x, x') \delta_{\ell'}(x') dx', \quad \text{or discretely} \quad \langle \mathbf{v}_p \rangle = \mathbf{C}_{v\delta} \cdot \mathbf{C}_{\delta\delta}^{-1} \cdot \boldsymbol{\delta}, \quad (14)$$

where the kernel, $K_{\ell\ell'}(x, x')$, is a simple function of the assumed 3D power spectrum given by equation (B14), while $\mathbf{C}_{\delta\delta}$ and $\mathbf{C}_{v\delta}$ are respectively the log density autocorrelation, and the mixed log density–velocity correlation given by

$$\mathbf{C}_{\delta\delta} \equiv (\langle \delta_i \delta_j \rangle)_{i=1\dots n, j=1\dots n}, \quad \mathbf{C}_{v\delta} \equiv (\langle v_i \delta_j \rangle)_{i=1\dots p, j=1\dots n}, \quad (15)$$

assuming we know the log-density at n points in space (p stands for the number of points at which we seek the velocity).

To obtain the density in real space along one LOS, it is possible to rely on the explicit Bayesian method once more, by using for the model, g , equation (6) or equation (8) with v_p given by equation (14). This ‘strong prior’ régime will be tested against simulations in Section 5.4.2. Of course, the Bayesian method could as well allow us to perform the simultaneous 3D reconstruction of the density field.

The constrained mean field machinery can also be used to reconstruct the 3D density field in redshift space (or in real space once the

⁴Hence we do not address here possible non-Gaussianity due to topological defects.

density along each LOS is deconvolved from redshift distortion), $\langle \delta^{(3D)} \rangle(x)$. This is particularly relevant at low spectral resolution which corresponds to the large-scale régime, where equation (13) can be directly used for $\delta_\ell(x)$. One obtains (equation B15)

$$\langle \delta^{(3D)} \rangle(x_\lambda) = \sum_\ell \int K_{\lambda\ell}^{(3D)}(x_\lambda, x'_\ell) \delta_\ell(x'_\ell) dx', \quad \text{or} \quad \langle \delta^{(3D)} \rangle = \mathbf{C}_{\delta^{(3D)}\delta} \cdot \mathbf{C}_{\delta\delta}^{-1} \cdot \delta, \quad (16)$$

where the kernel, $K_{\lambda\ell}^{(3D)}(x_\lambda, x'_\ell)$, is also a function of the assumed 3D power spectrum given by equation (B15). $\mathbf{C}_{\delta\delta}$ is given by equation (15), $\mathbf{C}_{\delta^{(3D)}\delta}$ is the mixed LOS-3D overdensity correlation given by $\mathbf{C}_{\delta^{(3D)}\delta} \equiv (\langle \delta_i^{(3D)} \delta_j \rangle)_{i=1\dots p, j=1\dots n}$.

3.3 Overlap between the two methods and connection with Wiener filtering

The above extrapolation technique is restricted to quasi-linear analysis in redshift space and unsaturated absorption lines, since it assumes a priori that the density is *known* along each LOS and that it is Gaussian distributed. As such, constrained mean fields methods cannot be applied directly to equation (1) which involves a double non-linear convolution over the underlying density both explicit (via n_{H1}) and implicit (via v_p). The Bayesian approach sketched in Section 3.1 is more general and makes less stringent assumptions. In particular, it should provide means of applying redshift distortion correction on the fly while accounting for temperature-induced blending. We none the less show that, for linear models, when the prior dominates, the extrapolation ability of equation (10) reduces to constrained mean field extrapolation, while, in contrast, in the zero prior limit, it reduces to Wiener filtering. We also show how the covariance of the prior log-density and velocity can be adjusted to fix a unique linear relationship between the sought density field and its redshift distortion.

Let us start from the explicit Bayesian method. If the prior is null, $\mathbf{M}_0 \equiv 0$, the error in the measurements negligible, $\mathbf{C}_d \approx 0$, the model linear, $g(\mathbf{M}) = \mathbf{G} \cdot \mathbf{M}$, equation (11) becomes

$$\langle \mathbf{M} \rangle = \mathbf{C}_0 \cdot \mathbf{G}^\perp \cdot (\mathbf{G} \cdot \mathbf{C}_0 \cdot \mathbf{G}^\perp)^{-1} \cdot \mathbf{D}. \quad (17)$$

When recovering the 3D density field from the measured density along the LOSs, $\mathbf{C}_0 \equiv \mathbf{C}_{\delta^{(3D)}\delta^{(3D)}}$, the linear operator \mathbf{G} operates then simply like a Dirac comb on a field η :

$$\mathbf{G}_\ell \cdot \eta \equiv \int \delta_D(\mathbf{x}_\perp - \mathbf{x}_{\perp\ell}) \eta(\mathbf{x}) d\mathbf{x}_\perp, \quad (18)$$

so that

$$\mathbf{C}_0 \cdot \mathbf{G}^\perp = \mathbf{C}_{\delta^{(3D)}\delta} \quad \text{and} \quad \mathbf{G} \cdot \mathbf{C}_0 \cdot \mathbf{G}^\perp = \mathbf{C}_{\delta\delta}, \quad \text{which implies for equation (17): } \langle \delta^{(3D)} \rangle = \mathbf{C}_{\delta^{(3D)}\delta} \cdot (\mathbf{C}_{\delta\delta})^{-1} \cdot \delta. \quad (19)$$

Equation (19) is identical to equation (16). Note incidentally that if the prior is null and the model linear, but if the errors in the measurements are accounted for, equation (11) becomes

$$\langle \mathbf{M} \rangle = \mathbf{C}_0 \cdot \mathbf{G}^\perp \cdot (\mathbf{G} \cdot \mathbf{C}_0 \cdot \mathbf{G}^\perp + \mathbf{C}_d)^{-1} \cdot \mathbf{D} = (\mathbf{G}^\perp \cdot \mathbf{C}_d^{-1} \cdot \mathbf{G} + \mathbf{C}_0^{-1})^{-1} \cdot \mathbf{G}^\perp \cdot \mathbf{C}_d^{-1} \cdot \mathbf{D}, \quad (20)$$

which corresponds to Wiener filtering (Wiener 1949; Zaroubi et al. 1995). In other words, when the model is linear, our method is equivalent to Wiener filtering applied to $\mathbf{M} - \mathbf{M}_0$. When we seek to invert for both δ and v_p (hence imposing a weak prior on the field),

$$\mathbf{M} \equiv (\delta, v_p), \quad (21)$$

The penalty function (corresponding to the log of the prior in equation 10) can be re-arranged (cf. equation B2):

$$(\mathbf{M} - \mathbf{M}_0)^\perp \cdot \mathbf{C}_0^{-1} \cdot (\mathbf{M} - \mathbf{M}_0) = (\mathbf{v}_p - \mathbf{C}_{v\delta} \cdot \mathbf{C}_{\delta\delta}^{-1} \cdot \delta)^\perp \cdot (\mathbf{C}_{vv} - \mathbf{C}_{v\delta} \cdot \mathbf{C}_{\delta\delta}^{-1} \cdot \mathbf{C}_{v\delta}^\perp)^{-1} \cdot (\mathbf{v}_p - \mathbf{C}_{v\delta} \cdot \mathbf{C}_{\delta\delta}^{-1} \cdot \delta). \quad (22)$$

The strong prior régime, mentioned in Section 3.2 and tested in Section 5.4.2, is therefore a subcase of equation (22) where

$$\mathbf{C}_{vv} \approx \mathbf{C}_{v\delta} \cdot \mathbf{C}_{\delta\delta}^{-1} \cdot \mathbf{C}_{v\delta}^\perp, \quad \text{implying} \quad \mathbf{v}_p \approx \mathbf{C}_{v\delta} \cdot \mathbf{C}_{\delta\delta}^{-1} \cdot \delta,$$

i.e., \mathbf{v}_p will take its most likely value, as was assumed in equation (14).

Both the explicit Bayesian method and the constrained mean field reconstruction require detailed description of a *prior* model for the large-scale structure of the IGM in order to fix \mathbf{M}_0 , \mathbf{C}_0 , $P_{3D}(\mathbf{k})$, plus additional relationships such as those sketched in Section 2. As mentioned earlier, these methods can be iterated with new priors measured in the reconstructed data, but we have not tested the convergence of such a scheme, and leave that to future work.

4 NUMERICAL SIMULATIONS

To test our methods we use two standard cold dark matter (CDM) N -body simulations. The gas distribution is derived from the DM distribution, using simple recipes described in Section 2 and based on previous works (e.g. Hui & Gnedin 1997; Nusser & Haehnelt 1999a). As discussed in the analysis of more realistic numerical simulations, taking fully into account the details of the gas dynamics is left for future work. Many aspects of the reconstruction problem do not strongly depend on the detail of the gas dynamics.

The simulations were run with a particle-mesh (PM) code, fully vectorized and parallelized on SGI-CRAY architecture with shared

Table 1. Characteristics of the N -body experiments.

Model	Ω_0	Λ	h	Γ	σ_8	N_p	L
S	1.0	0.0	0.5	0.5	0.51	$512 \times 256 \times 256$	$50 \times 25 \times 25$
B	1.0	0.0	0.5	0.5	0.51	$1024 \times 128 \times 128$	$800 \times 100 \times 100$

Model: 'S' and 'B' stand for 'small' and 'big' respectively.

Ω_0 : value of the density parameter of the Universe.

Λ : value of the cosmological constant.

h : parametrizes the Hubble constant, $H_0 = 100 h \text{ km s}^{-1} \text{ Mpc}^{-1}$.

Γ : shape parameter of the initial power spectrum (see, e.g. Jenkins et al. 1998 for details). σ_8^2 : the linear variance in the dark matter at the present time in a sphere of radius $8 h^{-1} \text{ Mpc}$ (to fix the normalization). N_p : size of the grid used to compute the potential and the forces; also the number of particles. L : dimensions of the rectangular periodic box in comoving Mpc.

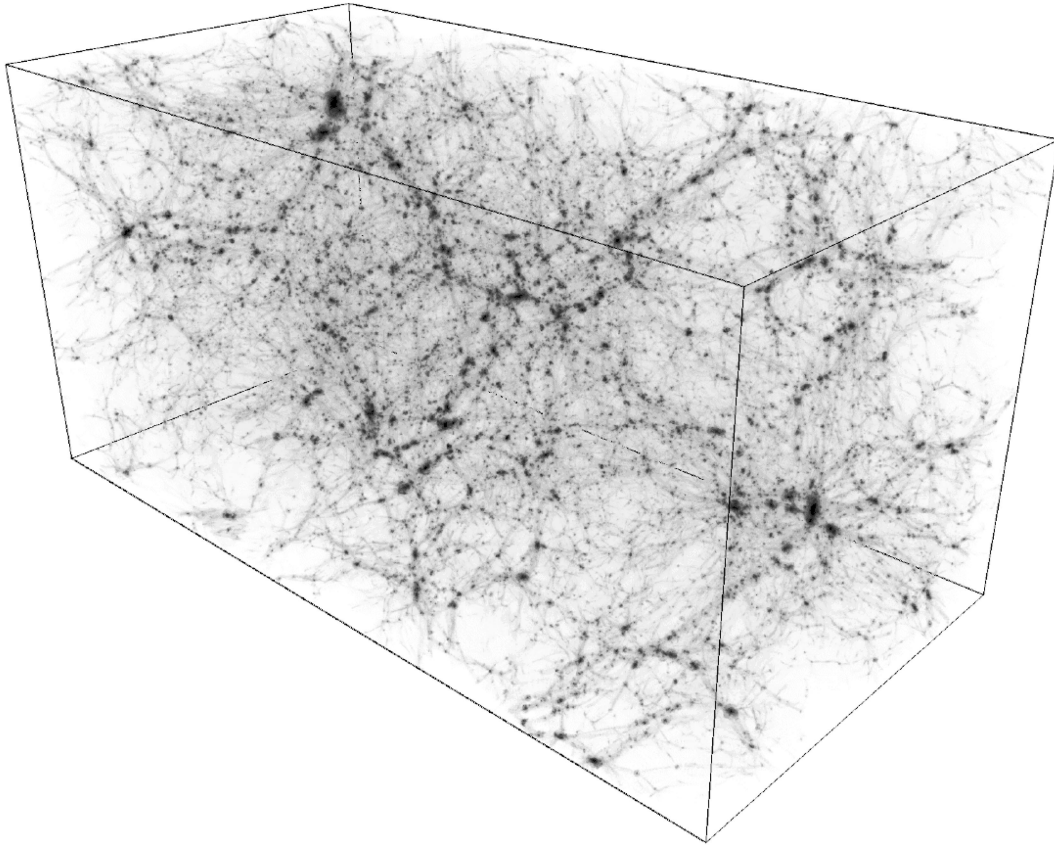


Figure 1. The dark matter distribution in the small simulation box, S, at $z = 2$ (see Table 1 and text). The colour scales roughly logarithmically with the projected density. Darker regions are denser.

memory.⁵ The characteristics of the simulations, S and B, which involve respectively ~ 32 and ~ 16 millions particles, are given in Table 1. The cosmological parameters are inspired from Jenkins et al. (1998). The particles were laid down on a mesh with the same shape as the grid used to compute the forces. Then the Zel'dovich (1970) approximation was used to perturb the positions of the particles and to set up Gaussian initial conditions with the appropriate power spectrum for standard CDM. This was done in a similar way as in the COSMICS package of Bertschinger (1995). To avoid effects of transients (e.g. Scoccimarro 1998), the simulations were started at high redshift $z = 255$ and evolved until the desired redshift, $z = 2$. Figs 1 and 2 display the corresponding DM distribution. A detailed analysis of the power spectrum and the variance of the density field measured in the simulations is presented in Appendix C.

The spatial comoving resolutions of simulations S and B are $\lambda_g \simeq 4.9$ and 40 km s^{-1} respectively, which correspond to physical resolutions ~ 8.5 and 68 km s^{-1} at $z = 2$. This is to be compared with the maximum possible pixel resolutions of the instruments available on

⁵This program is an improved version of an older code (Bouchet, Adam & Pellat 1985; Alimi et al. 1990; Moutarde et al. 1991; Hivon 1995). It uses for better performances a 'predictor-corrector' (e.g. Rahman 1964) implementation of the time-step (instead of the traditional 'leapfrog', e.g. Hockney & Eastwood 1981). It is still in construction, but available on request by e-mail at nic@iap.fr.

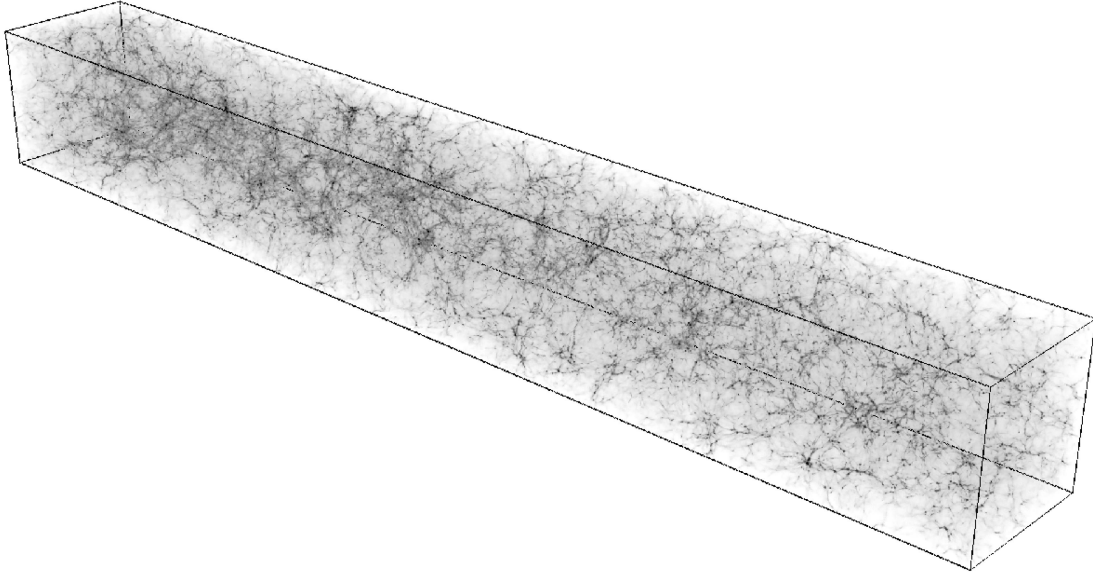


Figure 2. Same as Fig. 1, but for the large simulation box, B.

the VLT: UVES, $\lambda \approx 3 \text{ km}^{-1}$, and FORS, $\lambda \approx 100 \text{ km}^{-1}$. However, the actual resolution of the simulation depends on the physical parameter of interest, and is always worse than the mesh resolution. For density-related processes, we can expect the PM simulation to be sufficiently accurate at scales as small as $\sim 2\lambda_g$, although the dynamics can actually be contaminated by softening of the forces on scales as large as $6\lambda_g$ (Bouchet et al. 1985). For velocities, which are quite sensitive to resolution, numerical comparisons between PM simulations and higher resolution codes show that results are correct to within ~ 25 per cent at scales close to λ_g (e.g. Colombi 1996). Concerning the gas dynamics, density fluctuations are expected to be damped out below the Jeans length, and therefore it is not necessary to have a spatial resolution much better than this cut-off scale. For example, the thorough analysis of Gnedin & Hui (1998) shows that this scale is of the order of $50\text{--}100 h^{-1}$ comoving kpc, i.e., $5\text{--}10$ comoving km s^{-1} . This roughly corresponds to the spatial resolution of the S simulation (at least for density-related quantities). In this respect, the resolution of the B simulation is not high enough, and this simulation is only used to test reconstruction of weakly non-linear structures.

In addition to small-scale softening and limited resolution, discreteness effects represent another source of concern, particularly in underdense regions. We apply adaptive Gaussian smoothing to the particle distribution as follows. The mean quadratic distance, d_i , between each particle, i , and its six nearest neighbours is computed. This sets a smoothing length, $\ell_i = d_i$, i.e., the Gaussian filter associated to particle i is $W_{\ell_i}(r) \propto \exp(-r^2/2\ell_i^2)$ within $3\ell_i$ after appropriate renormalization. In practice, the smoothed density (or mass-weighted velocity) is computed on a grid chosen here to be the same as the simulation grid. Each cell, j , is subdivided in N^3 subpixels, k_j , corresponding to positions x_{k_j} , with $N = 3$. The contribution of particle i to the grid site j writes

$$C_{j,i} \propto \sum_{k_j, |r - x_{k_j}| \leq 3\ell_i} W_{\ell_i}(|r - x_{k_j}|), \quad (23)$$

with the appropriate normalization $\sum_j C_{j,i} = m_i$, where m_i is the mass of particle i .

5 APPLICATION

In this section we apply the methods discussed in Section 3 to simulated Lyman- α spectra extracted from the N -body simulations (using equation 6).

Our preliminary analyses are organized as follows. In Section 5.1 we give some details on the models and the priors used for both the Bayesian method and the constrained mean field reconstruction. Section 5.2 deals with 3D reconstruction of the density field. We first test the constrained mean field method in a régime where the density along each LOS is supposed to be known. Next, we test the Bayesian approach. The latter method does not rely on such a strong prior for the density, and is first applied to the large-scale régime discussed in Section 2.2, where thermal broadening can be neglected. Moreover, redshift distortion is not taken into account. In Section 5.3 we apply the Bayesian method to constrain the equation of state of the gas. We consider the small-scale régime as discussed in Section 2.2, but neglect redshift distortion again for the sake of simplicity, although peculiar velocity effects should realistically be accounted for. These velocities are dealt with in Section 5.4, which assume in turn that the equation of state of the IGM is well constrained. We analyse the efficiency of velocity reconstruction versus number of LOSs, and test Bayesian reconstruction in the frameworks of strong and floating priors.

The reader will notice that for each problem considered, we neglect in turn either redshift distortion or thermal broadening. Accounting simultaneously for both effects can in principle be achieved with the explicit Bayesian method or a combination with the constrained mean

field reconstruction. However, our main goal here was to illustrate the method and to pin down various effects at each step of the reconstruction, concentrating on one particular property of the IGM, such as the structures of the 3D density field, the equation of state, or redshift distortion. More general applications will be developed in future work.

5.1 The priors

5.1.1 Explicit Bayesian method

The Gaussian Bayesian prior (equation 10) is fully described by the first two moments: the prior choice for the parameters of the model, \mathbf{M}_0 , and its covariance, \mathbf{C}_0 .

For the model we choose the following combination of fields and discrete parameters:

$$\mathbf{M} = [\gamma(x, \mathbf{x}_\perp), v_p(x, \mathbf{x}_\perp), \bar{T}, \beta]. \quad (24)$$

Function $\gamma(x, \mathbf{x}_\perp)$ is defined as

$$\frac{\rho_{\text{DM}}(x, \mathbf{x}_\perp)}{\bar{\rho}_{\text{DM}}} = D_0(x, \mathbf{x}_\perp) \exp[\gamma(x, \mathbf{x}_\perp)], \quad (25)$$

so that positivity of density is insured. Here, $D_0(x, \mathbf{x}_\perp)$ is an arbitrary function (specified later) which fixes the value of the prior for $\rho_{\text{DM}}(x, \mathbf{x}_\perp)/\bar{\rho}_{\text{DM}}$, when $\gamma(x, \mathbf{x}_\perp) = \gamma_0 \equiv 0$. Note that $A(z)$ is assumed to be known throughout the paper.

For the prior, we take

$$\mathbf{M}_0 = [0, 0, \bar{T}_0, \beta_0], \quad (26)$$

where the values of \bar{T}_0 and β_0 will be given in Section 5.3.

We derive the prior covariance operator \mathbf{C}_0 either in an ad hoc manner (Sections 5.2.2, 5.3 and 5.4.2) or from the simulations (Section 5.4.3). In the first case, $\mathbf{C}_{\gamma\gamma}$ is chosen to obey

$$\mathbf{C}_{\gamma\gamma}(x, x', \mathbf{x}_\perp, \mathbf{x}_\perp') \equiv \sigma_\gamma^2 \exp\left(-\frac{|x - x'|}{\xi_x}\right) \exp\left(-\frac{|\mathbf{x}_\perp - \mathbf{x}_\perp'|}{\xi_T}\right), \quad (27)$$

where ξ_x and ξ_T are natural lengths in the inversion and govern the level of smoothness of the reconstruction. Typically, ξ_T will be of order of the mean transverse distance between two LOSs. The optimal choice for ξ_x depends on the problem considered. If peculiar velocity effects are neglected, ξ_x can be taken as small as the maximum scale between spectral resolution and Jeans length (Sections 5.2.2 and 5.3). In that case, no small-scale information is lost along the LOSs. However, when redshift distortion is to be taken into account (e.g. Section 5.4.2), it is necessary to have a smoother prior to stabilize the inversion, typically the length marking the transition toward the non-linear régime (in other words, the typical size of clumps).

The parameter σ_γ may, if required, depend on position. On average, it corresponds roughly to the variance of γ in a rectangle of volume $\xi_x \xi_T^2$. It governs indirectly by how much the reconstructed field, $\langle \mathbf{M} \rangle$, is allowed to float around the prior \mathbf{M}_0 while solving equation (11) with the iterative method detailed in Appendix A. When peculiar velocity effects are neglected, this parameter can be taken to be rather large, of the order of 0.2. Otherwise, the inversion process is more complicated: details will be given in Section 5.4.2. Exponential correlation functions turned out to be more appropriate than Gaussian ones in order to recover filamentary structures: the covariance kernel given in equation (27) is steeper, which allows us to take into account high-density fluctuations.

5.1.2 Constrained mean field reconstruction priors

The constrained mean field reconstruction method, applied in Sections 5.2.1, 5.4.1 and 5.4.2, also requires values for the prior covariance matrix \mathbf{C}_0 , which is taken to be those measured in the simulations, as detailed in Appendix B. Some of the biases involved in this choice are discussed in Section 5.2.3.

5.2 Large-scale structures: tomography of the IGM

We apply the two methods described in Section 3 to recover the large-scale structures in simulation B. For this purpose, we use a network of equally separated LOSs, along which we simulate spectra in accordance with equation (6) (as shown in Fig. 5) while varying the separation. We proceed in two steps: we first ignore all issues related to finite signal-to-noise ratios (S/N), thermal broadening or line saturation, and use constrained mean fields to extrapolate the density away from the LOSs, assuming that this latter is fully determined along the LOSs (Section 5.2.1); we then illustrate the Bayesian technique, which does not suppose that the density along the LOSs is known (Section 5.2.2). In the latter case, only the large-scale régime is considered [i.e., the régime (ii) discussed in Section 2.2], and redshift distortion is neglected ($v_p = 0$). Section 5.2.3 discusses shortcomings of the two methods and realistic extensions.

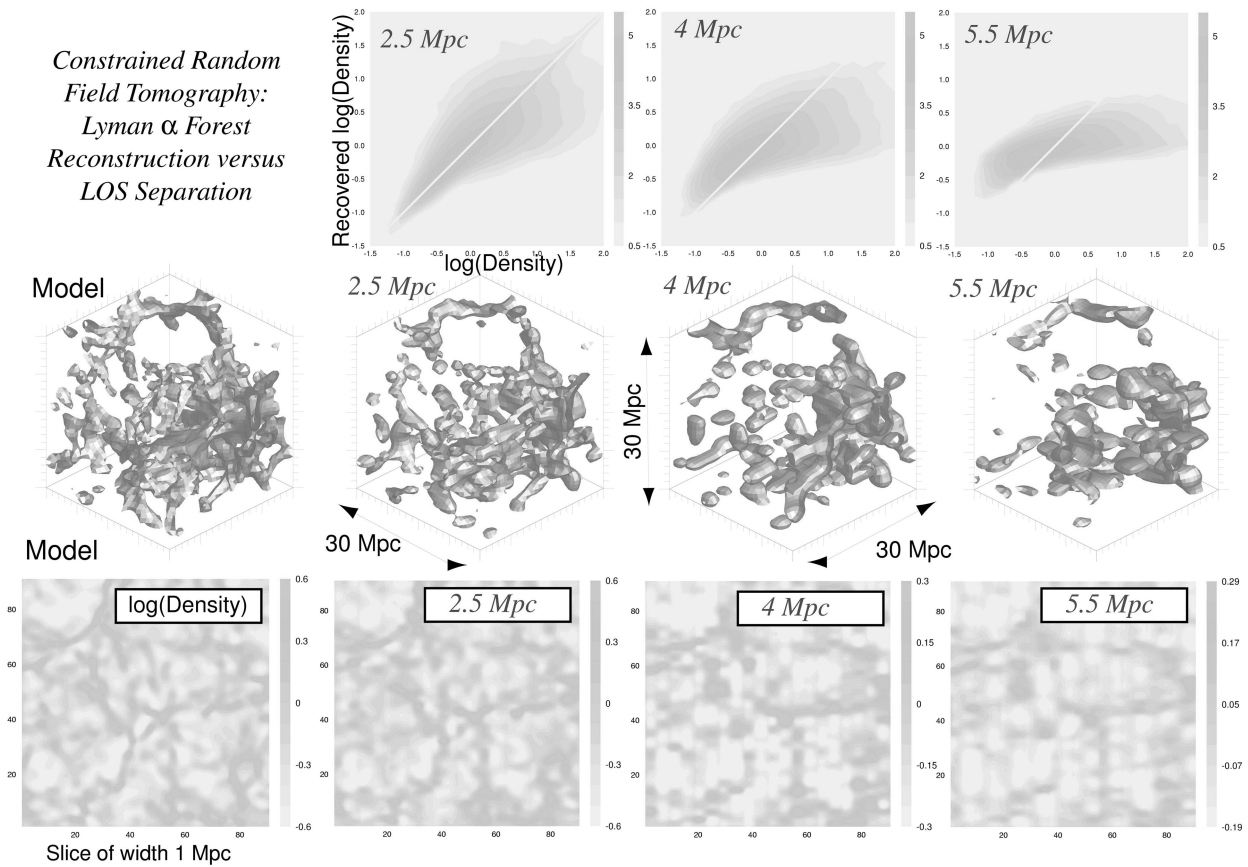


Figure 3. *Top panels, from left to right:* The recovered log density versus the real (simulated) log density as a function of the distance between the LOSs, L_{LOS} , as labelled: as expected, the bias increases with L_{LOS} ; *Middle panels, from left to right:* the model and the reconstructed density for $L_{\text{LOS}} = 2.5, 4$ and 5.5 Mpc comoving; *Bottom panels, from left to right:* a slice of $1 \times 80 \times 80$ Mpc across the simulation and the reconstructed fields (the scale on the panels is in pixels). Most of the small-scale structures are lost in the reconstructed field. The large-scale topology is, however, recovered. The rounded features in the reconstructed density are an artefact of the interpolation method.

5.2.1 Constrained mean field

Let us first consider redshift space and assume that we have derived the density on each LOS using for example equation (13). Recall that the most likely 3D density away from the LOS obeys equation (16). The covariance matrix of the prior, $\mathbf{C}_0 = \mathbf{C}_{\delta\delta}$, is shown on the top of the bottom right panel of Fig. 6. We present the results of a reconstruction of part of simulation B in Fig. 3. For this figure, we used the discrete form of equation (16), on a regular network of overlapping subgrids of size $20 \times 20 \times 20$ pixels such that the centres of adjacent subgrids are separated from each other by 10 pixels. The value of the reconstructed density on one pixel is obtained by a weighted interpolation of the recovered density on each subgrid containing this pixel, the weight being inversely proportional to the distance of the pixel from the centre of the subgrid considered. This procedure ensures smoothness of the reconstruction, while keeping the size of the matrices reasonable. The top panels of Fig. 3 illustrate the bias in the extrapolation procedure as we vary the distances between LOSs, the middle panels display the 3D reconstructed iso-log densities corresponding to $\delta = 0.2$, while the bottom panels show a slice through this field. The large-scale filaments are recovered for all separations investigated, but small-scale structures disappear beyond 2.5 Mpc comoving of separation. The topography of the structures is well described. As expected, the density is poorly recovered for the largest separations.

5.2.2 Bayesian reconstruction: line saturation and finite signal-to-noise ratio (S/N)

Choosing simply $D_0 \equiv 1$ in equation (25), our model g , on pixelized data, reads (equation 8 with $v_p = 0$; see also Appendix D1.2)

$$g_{i\ell}(\gamma) = A(\bar{z}) \exp[\alpha \gamma (w_{i\ell}, x_{\perp\ell})], \quad (28)$$

with α fixed equal to 1.7. Here, $w_{i\ell}$ is the velocity at bin i corresponding to the LOS labelled ℓ , and $\gamma(x, x_{\perp})$ is the only parameter for which the prior covariance is given by equation (27). The parameters σ_γ , ξ_x and ξ_r are respectively chosen equal to 1, twice the resolution and 1.5 times the distance between LOSs. The matrix \mathbf{G} is given in Appendix D1.2. Errors in the simulated data are modelled as follows. We assume that they are uncorrelated, so that the covariance error matrix \mathbf{C}_d is diagonal, with elements given by

$$\sigma_\tau^2 \equiv \frac{\sigma_F^2}{F^2} \approx \frac{1}{(S/N)^2} + \frac{\sigma_0^2}{F^2} = \frac{1}{(S/N)^2} + \sigma_0^2 \exp(2\tau), \quad (29)$$

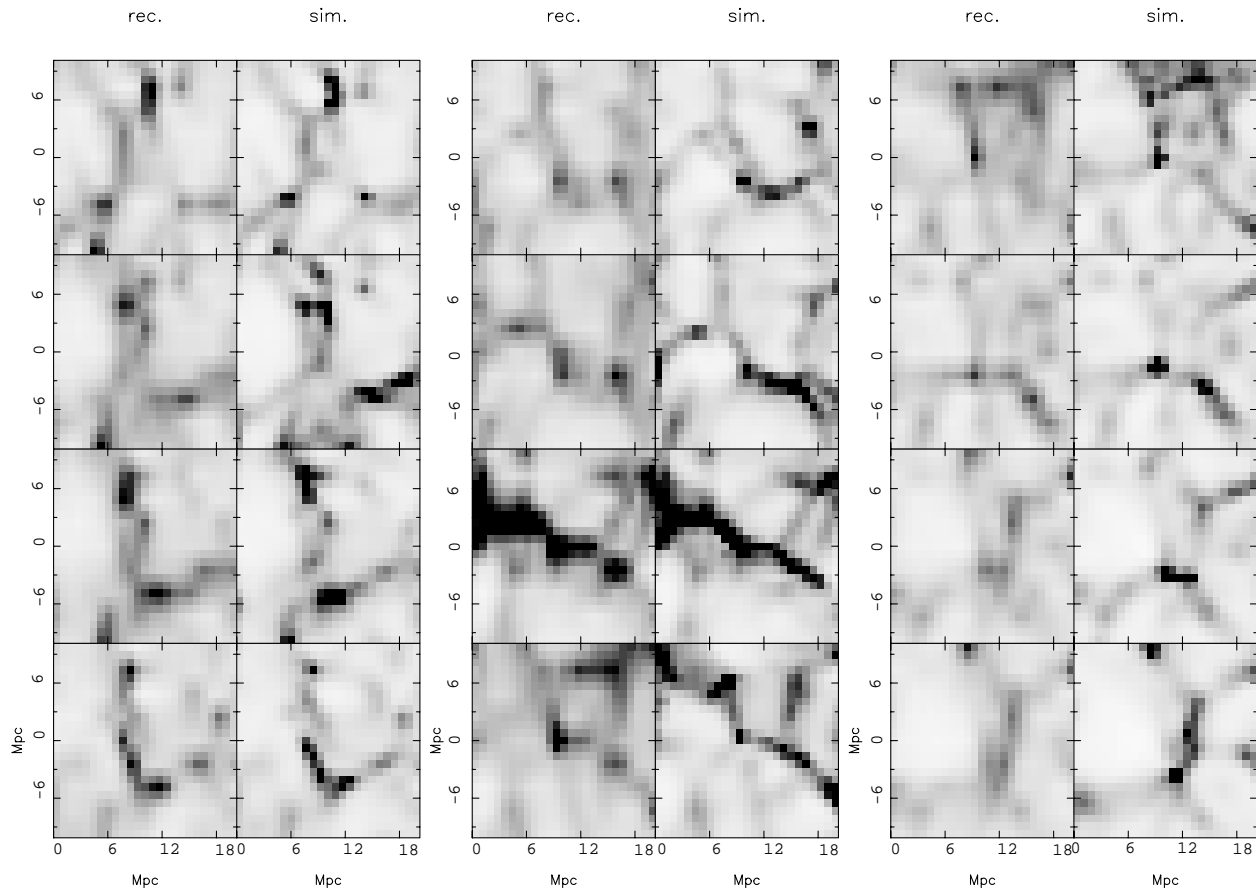


Figure 4. Density contrast reconstruction using the Bayesian algorithm from a set of 9×9 lines of sight taken through simulation B. The distance between two adjacent lines of sight is equal to 2.4 Mpc comoving. Each panel represents respectively on the left the reconstruction and on the right the simulation. Dark regions correspond to overdense regions. The filaments are well recovered.

since the observed flux is simply: $F(w) = \exp[-\tau(w)]$. Equation (29) states that the error on the flux has two origins: a constant S/N component and a residual instrumental noise, σ_0 , which dominates at large optical depth. In the inversion illustrated in Fig. 4, we use an S/N of 25 and a residual error of magnitude 0.01.

The reconstruction of filamentary structures is effective only in the régime where the distance between LOSs is of the order of 1–3 Mpc comoving. Beyond this limit, the isotropic method presented here is insufficient to recover the structure of the IGM (such anisotropic features may be described by higher order correlation functions and stronger assumptions relying on a prior different from equation 10). Inherent to the method is the limitation that density fluctuations at scales smaller than the separation between LOSs are damped out by the reconstruction. Also, the probability to intersect a given strong overdensity is inversely proportional to the amplitude of the overdensity. In other words, the information regarding rare high overdensities is simply not sampled enough by the LOSs. A related effect is induced by flux saturation in the spectra depending on the spectral resolution and the S/N. For instance, optical depths of $\tau = 5$ or 10 will correspond to very different overdensities but very similar (≈ 0) fluxes. Note finally that for simplicity we have made use of Gaussian line profiles, when Lorentzian would have been more appropriate.

5.2.3 Discussion

In the reconstruction of Section 5.2.1, the density is assumed to be known along the LOSs, together with the covariance matrix of the 3D log-density field. At low spectral resolution, we may neglect both thermal broadening and peculiar velocities, and use equation (13) to determine directly the density in redshift space from the Lyman α forest along each LOS. At high spectral resolution, thermal debroadening and redshift distortion deconvolution could in principle be achieved simultaneously with the explicit Bayesian method or a combination of the Bayesian method with the constrained mean field reconstruction, as discussed in Section 3.2 and shown below.

Note also that our prior for the 3D covariance matrix in Section 5.2.1 is optimal: it is measured directly in the simulation. In that sense, our reconstruction is biased, since we use part of the correct answer in advance. Moreover, we go beyond Gaussian linear approximation, since we work on \log -density, which contributes to improve the reconstruction even more. In real observations, we would not have a prior as good as that chosen here at our disposal. However, as shown in Section 5.2.2, the results from the explicit Bayesian reconstruction, which rely

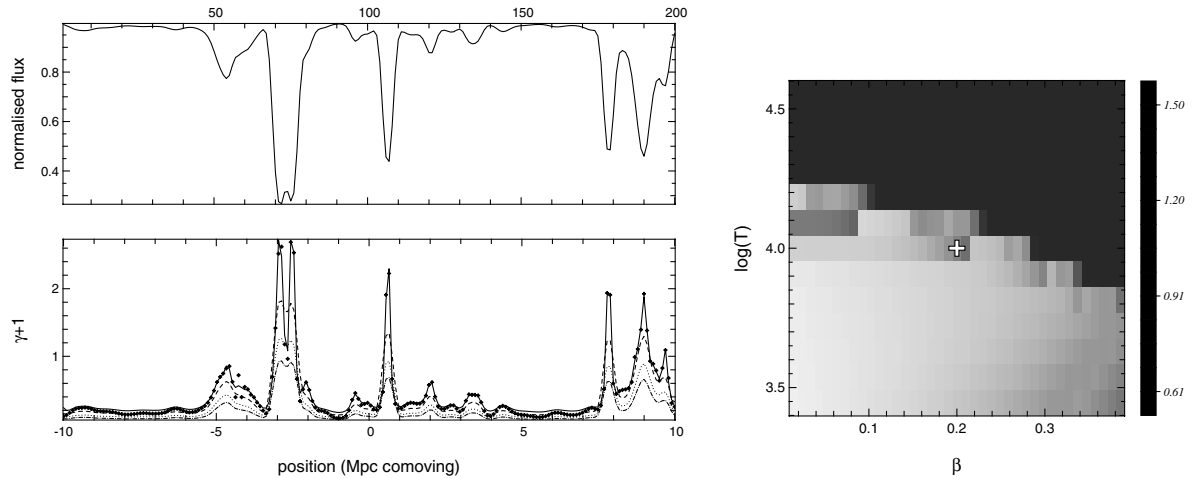


Figure 5. *Left-hand panels:* Inversion using different equations of state. The upper panel shows a portion of simulated spectrum through S. The equation of state used corresponds to equation (3) with $\bar{T} = \bar{T}_t \equiv 10^4$ K, $\beta = \beta_t \equiv 0.2$. Peculiar velocities are not considered. The lower panel shows the simulated density as black dots. The density recovered using the same equation of state is plotted as a solid line; it is apparent that even the internal structure of absorption blends is recovered. Other curves correspond to the results of inversions using various lower values of \bar{T} at fixed $\beta = 0.2$. The effect of lowering \bar{T} is to give smaller values for reconstructed density with a reduced $\chi^2 < 1$. If, on the contrary, $\bar{T} > T_t$, one obtains $\chi^2 \gg 1$. *Right-hand panel:* Map of convergence ($\chi^2 < 1$) or divergence ($\chi^2 \gg 1$) for inversions using equation (30) with different values of \bar{T} and β . The LOS is the same as in the left-hand panels.

on a much weaker prior, equation (27), give very similar results to the constrained mean field reconstruction. This shows that the non-linear features present in the measured correlations do not play an important role in our ability to carry out the inversion on the scales explored here. Finally, it may be worth mentioning again that the methods should be iterated, using for new priors and covariance matrixes the measured ones in the reconstructed field.

5.3 Small scales: the IGM temperature

We now aim to determine the equation of state of the IGM by considering the inversion of a single LOS observed at high spectral resolution [régime (i) in Section 2.2]. The inversion of the density, velocity and temperature fields from a single LOS is not unique (Hui & Rutledge 1999; Theuns et al. 1999). Indeed, the same spectrum can be reconstructed with different equations of state and density distributions, as illustrated by Fig. 5. Neglecting peculiar velocities for the sake of simplicity ($v_p = 0$), the problem reduces to the determination of two parameters \bar{T} and β and one unknown field, γ . The simultaneous determination of these parameters *and* the field remains a degenerate problem. As detailed in Appendix D1.1, our model, g , on pixelized data reads, from equation (6),

$$g_{i\ell}(\gamma) = A(\bar{z})c_1 \int \int \left(\int_{-\infty}^{+\infty} \{D_0(x, \mathbf{x}_\perp) \exp[\gamma(x, \mathbf{x}_\perp)]\}^{\alpha-\beta} \exp \left[-c_2 \frac{(w_{i\ell} - x)^2}{\{D_0(x, \mathbf{x}_\perp) \exp[\gamma(x, \mathbf{x}_\perp)]\}^{2\beta}} \right] dx \right) \delta_D(\mathbf{x}_\perp - \mathbf{x}_{\perp\ell}) d^2\mathbf{x}_\perp. \quad (30)$$

Here, $A(\bar{z})$ is arbitrarily fixed to $A(\bar{z}) = 0.7$ as explained in Section 5.1.1, $\alpha = 2 - 1.4\beta$ (equation 4), and c_1 and c_2 are functions of \bar{T} (equation 7). The function $D_0(x, \mathbf{x}_\perp)$ is chosen to be

$$D_0(x, \mathbf{x}_\perp) = \left[\frac{\tau_\ell(w \equiv x)}{A(\bar{z})} \right]^{1/\alpha}. \quad (31)$$

The prior covariance matrix $\mathbf{C}_{\gamma\gamma}$ is given by equation (27) with $\xi_T \rightarrow \infty$. Here ξ_x and σ_γ are chosen equal to 0.2 Mpc comoving and 0.2.

We conduct our analyses as follows. We first simulate a spectrum along one LOS with a given *real* pair (β, \bar{T}) . The noise matrix \mathbf{C}_d is the same as in Section 5.2.2 with a $(S/N, \sigma_0) = (50, 0.05)$. We then invert this LOS for $\gamma(x)$, while varying (β, \bar{T}) over a given range of realistic values. In that sense, the only *effective* parameter in the inversion is the field γ . For each value of (β, \bar{T}) , we compute the reduced χ^2 , i.e., $[\mathbf{D} - g(\mathbf{M})^\perp \cdot \mathbf{C}_d^{-1} \cdot [\mathbf{D} - g(\mathbf{M})]]$ in equation (10), as shown in the right-hand panel of Fig. 5. The value of (β, \bar{T}) is shown by a white cross. The (β, \bar{T}) plane is divided into two regions separated by a straight borderline, one with $\chi^2 \gg 1$ (corresponding to large values of \bar{T}) and the other one with $\chi^2 \leq 1$. This arises because the absorption lines are indeed thermally broadened and resolved. When $\bar{T} > \bar{T}_t$, the absorption features in the data are narrower than the model and cannot be fitted anymore.

As expected, the real parameters stand on the borderline between convergence and divergence: these parameters correspond to a good fit. We cannot however distinguish – using a χ^2 criterion – between pairs of (β, \bar{T}) on this borderline. Even though the degeneracy is not completely lifted, this analysis provides a complementary method to the standard techniques of Voigt profile fitting (see Schaye et al. 1999 and Ricotti et al. 2000) to measure the mean properties of the IGM and its cosmological evolution. The application of our method to real data is developed to a companion paper (Rollinde, Petitjean & Pichon, submitted).

Note finally that, for close enough LOSs (e.g., multiple lensed QSO images) we might in theory be able to investigate the small-scale 3D properties of the IGM, while accounting for thermal broadening.

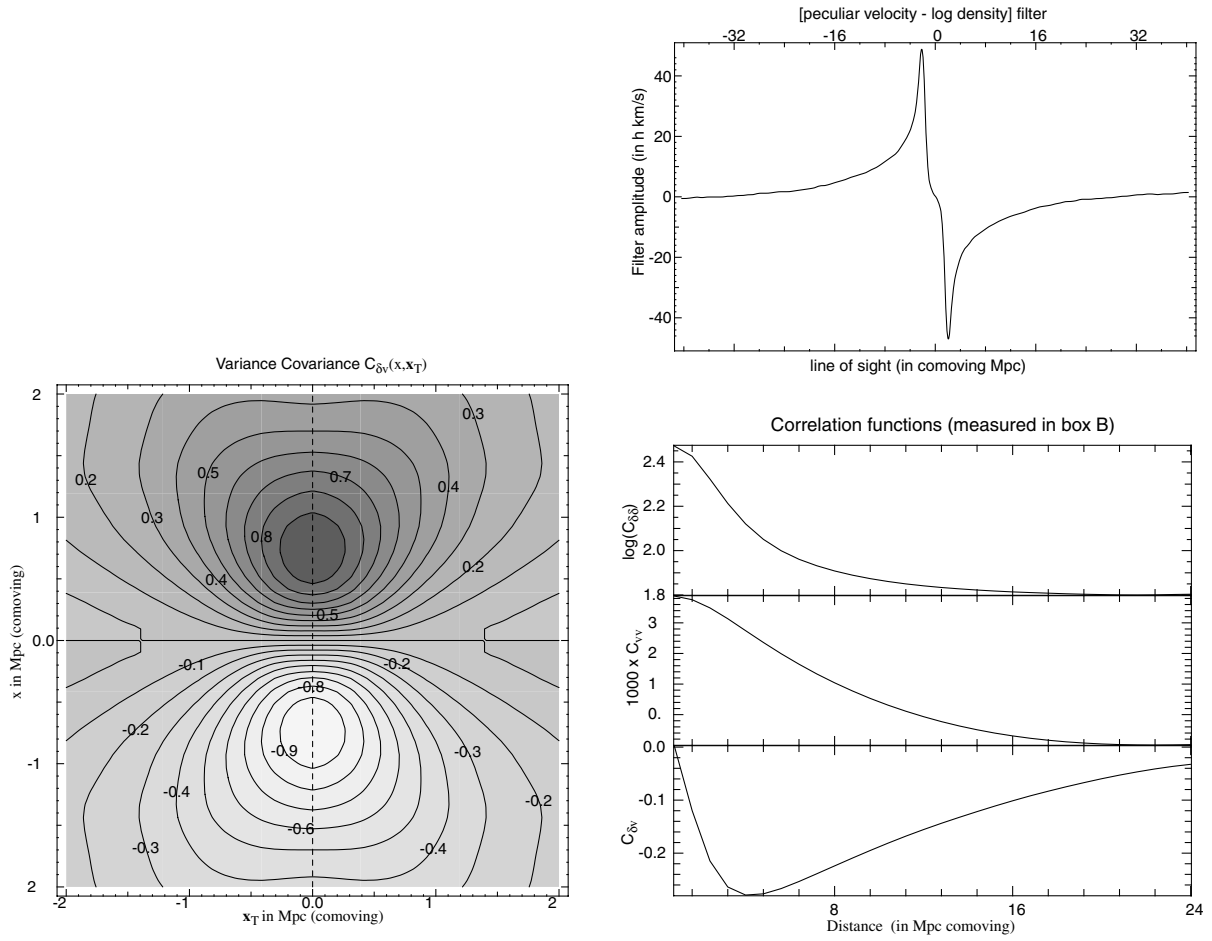


Figure 6. *Left-hand panel:* the 3D correlation function, $C_{\delta\delta}(x, x_{\perp})$, measured in simulation S. *Top right panel:* the filter $K^{(v)}$ required to compute the most likely velocities along one LOS (equation 14 with $\ell = \ell' = L = 1$). The width of the filter shows that the peculiar velocity has two natural scales, as discussed in the main text. *Bottom right panel:* the 1D LOS correlation functions: top subpanel: $\log(C_{\delta\delta})$; middle subpanel: C_{vv} ; bottom subpanel: $C_{\delta v}$.

5.4 Redshift distortion

Recall that in this section, for the sake of simplicity, we assume that the equation of state of the IGM is known.

There are several issues to address here. The optical depth along a bundle of LOSs does not constrain uniquely the corresponding velocity field. This would require the knowledge of the full 3D density distribution, together with the assumption that linear dynamics applies. Thus we first investigate how increasing the number of measured LOSs, or changing the mean separation between them, improves the likelihood of the corresponding realization of the constrained velocity field for a given density field along the bundle (Section 5.4.1). We then turn to the problem of deconvolving the optical depth in real space, but conduct a preliminary analysis on a *single* LOS. We test two approaches. The first approach is a strong prior inversion (Section 5.4.2), i.e., it relies on the Bayesian formalism, while assuming that the velocity field takes its most likely value. The second method allows the velocity field to float around this most likely value (Section 5.4.3). Finally, we discuss the limitations of the present work and possible improvements (Section 5.4.4).

Let us briefly describe the filters and correlation function involved. Fig. 6 (left-hand panel) displays the 3D correlation function, $C_{\delta\delta}(x, x_{\perp})$, measured in simulation S. It is antisymmetric along the LOS, and symmetric orthogonally. The top right panel shows the 1D filter, $K^{(v)}(x, y)$ (equation 14 with $\ell = \ell' = L = 1$), which was in practice computed according to the prescription sketched in Appendix B. This antisymmetric filter presents two characteristic scales: a strong peak at ≈ 2 Mpc (comoving) and broad wings up to ≈ 20 Mpc. This implies that the most likely velocity at a given point will depend on the local density *and also significantly* on the density further away (up to ≈ 20 Mpc). Transversally, the shape of the 3D cross-correlation function, $C_{\delta v}(x, x_{\perp})$, which vanishes near the line $x = 0$, implies that the density away from a given point will dominate the local velocity field.

5.4.1 Most likely velocity versus LOS separation and the number of LOSs

In this subsection we assume temporarily that the log-density field is known along a bundle of LOSs. In the framework of constrained mean field (Section 3.2), equation (14) gives the relationship between the most likely velocity along a given bundle of LOSs and the corresponding log-density.

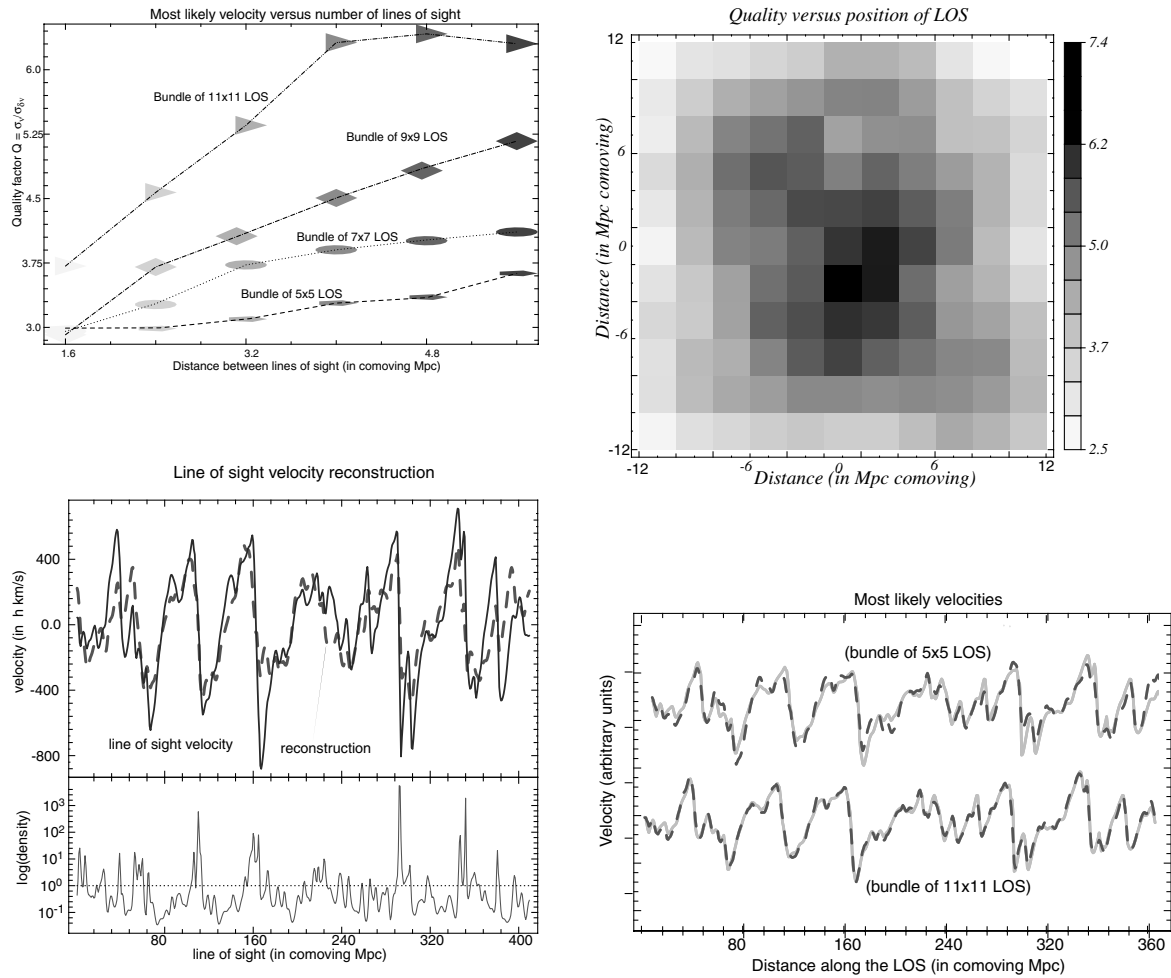


Figure 7. *Top left panel:* quality of the reconstruction (equation 32) versus LOS separation and the number of LOSs. Increasing the sampling on the sky decreases the dispersion between the constrained most likely velocity and the measured velocity as discussed in the text. Note the saturation for 11×11 LOSs at a separation of ≈ 5 Mpc. *Top right panel:* isocontour for the quality of the reconstruction projected on the sky for a bundle of 11×11 LOSs, separated by 2.4 Mpc comoving. Note that the reconstruction obviously works better for the central LOSs. *Bottom left panel:* in simulation B, most likely velocity constrained by a single LOS. The solid line on the upper subpanel corresponds to simulated velocity, and the dashed one to the reconstructed velocity. The simulated density is displayed in the lower subpanel. *Bottom right panel:* solid lines: simulated velocities along the centre of a bundle of 5×5 LOSs or 11×11 LOSs; dashed lines: corresponding recovered velocities.

Let us define the quality factor, Q , as

$$Q \equiv \frac{\sigma_{v_p}}{\sigma_{\delta v_p}} = \sqrt{\frac{\langle v_p^2 \rangle}{\langle (v_p - v_{\text{rec}})^2 \rangle}}, \quad (32)$$

where v_{rec} is the reconstructed velocity. Parameter Q measures the inverse residual misfit in units of the variance for the velocity. We show in Fig. 7 (top left panel) that this number increases with the number of LOSs sampling the sky, as expected. However, Q increases as well with the distance between LOSs until it reaches a maximum, which might sound confusing. This can be easily understood by examining the left-hand panel of Fig. 6. In fact, a bundle of LOSs constrains the transverse 3D velocity distribution *at intermediate scales*, as a result of a competition between short-range and long-range correlations.

(i) High-frequency structures are read from the LOS through the two strong peaks along the x coordinate axis in the left-hand panel of Fig. 6 (at approximately ± 0.8 Mpc). Other LOSs can in principle contribute to small scales, but only if they are found very close to the LOS of interest (i.e., with $\mathbf{x}_\perp \approx 0$).

(ii) Low 3D frequency features are mainly sampled by LOSs away from the LOS of interest, due to the significant tails present on $\mathbf{C}_{v\delta}$ at scales as large as ~ 20 Mpc, as illustrated by the top right panel of Fig. 6. This effect is three-dimensional, i.e., in *all directions*: it thus provides information on the structures transverse to the LOS.

(Note that in this discussion, we implicitly assumed that $\mathbf{C}_{\delta\delta} \approx \text{identity}$ in equation 14. Taking into account the real contribution of matrix $\mathbf{C}_{\delta\delta}^{-1}$ would simply boil down to smoothing the density with an isotropic filter, which has no effect on our qualitative conclusions.)

The competition between effects (i) and (ii) fixes an optimal separation between the LOSs as a function of their number. From the top

left panel of Fig. 7, we see, for example, that the optimal separation is 5 Mpc for a bundle of 11×11 LOSs. For a bundle with a smaller number of LOSs, the optimal separation becomes larger, so that the tails of $\mathbf{C}_{v\delta}$ are still fully sampled (but with a sparser binning and thus a smaller quality factor).

The bottom right and left panels of Fig. 7 compare the velocity along one LOS measured in the simulation to the reconstructed one by applying equation (14) to bundles of various sizes (1×1 , 5×5 and 11×11) distributed uniformly on the sky (from simulation B), with a mean separation of 2.5 Mpc. With only one LOS, the reconstructed velocity does not account in detail for small structures, although it seems to match well large-scale flows in the example studied here. Increasing the number of LOSs significantly improves the reconstruction: with a bundle of 11×11 LOSs, the reconstruction almost perfectly matches the simulation.

An important outcome of this analysis is that since the optimal separation between LOSs is rather large (a few Mpc), the small-scale information in the reconstruction is only contained in the LOS of interest. Therefore, having high-resolution spectra on all the LOSs is not required: a survey dedicated to real-space reconstruction should provide a high-resolution spectrum together with a set of low-resolution spectra separated by distances smaller than or of the order of $\approx 4\text{--}5$ Mpc comoving. Note that Q was computed while averaging over the whole bundle: the quality of the reconstruction in fact depends on the position of the LOS in the bundle, as illustrated in the top right panel of Fig. 7. Obviously, the quality factor is optimal at the centre of the bundle: the high-resolution spectrum should be located there.

We assumed here that the 3D covariance matrices needed for the reconstruction were known. In fact, we used the best possible guess for them, since they were derived from direct measurement in the simulation. In reality, we would have to proceed iteratively: for a given power spectrum, we could recover the 3D density, compute perturbatively the corresponding 3D velocity field, and derive a new covariance matrix until convergence is achieved. We have not demonstrated here that this procedure is convergent. This is certainly a possible shortcoming of the procedure.

5.4.2 Strong prior inversion

Let us now try to deconvolve the density in real space along *one* LOS. A combination of the general Bayesian method and the constrained mean field technique is implemented: the constrained mean field method allows us to relate the unknown field v_p to γ , imposing that the peculiar velocity takes its most likely value, but the recovery of γ is still based on the Bayesian method. Our model, $g_i(\gamma)$, is now

$$g_i(\gamma) = A(\bar{z})c_1 \int_{-\infty}^{+\infty} \{D_0(x) \exp[\gamma(x)]\}^{\alpha-\beta} \exp\left[-c_2 \frac{[w_i - x - v_p(x)]^2}{\{D_0(x) \exp[\gamma(x)]\}^{2\beta}}\right] dx, \quad (33)$$

with the supplementary assumption that the peculiar velocity in equation (33) equals the most likely velocity (Appendix B):

$$v_p(x) = \langle v \rangle \equiv \int K^{(v)}(x, y) \gamma(y) dy, \quad \text{where} \quad K^{(v)}(x, y) \equiv \frac{1}{2\pi} \int e^{ik_x(x-y)} \frac{P_{v\delta,1D}(k_x)}{P_{\delta\delta,1D}(k_x)} dk_x. \quad (34)$$

The unknown parameter remains the density contrast. The prior for the density is chosen as $D_0 \equiv 1$ so that $\gamma = \delta$. For the filter $K^{(v)}(x, y)$ we use a simple analytic fit of the function $K^{(v)}(x, y)$ measured in the simulation as explained in Appendix B1.1. The derivation of the different vectors and matrices involved in this case is sketched in Appendix D2.1. The practicalities involves fixing appropriately the parameters (σ_γ, ξ_x) in equation (27) ($\xi_T \equiv \infty$ for a single LOS) for the minimization procedure detailed in Appendix A to converge while providing as accurate reconstruction as possible. To stabilize the inversion, we need to take for ξ_x a value close to the correlation length, $\xi_x = 1$ Mpc. With a larger value of ξ_x , the inversion is still stable but makes the reconstructed density field too smooth, while a smaller value of ξ_x makes the inversion unstable. The choice of σ_γ , which fixes the amount of variations allowed around the prior, is more delicate. A small value of σ_γ makes convergence easier, but does not leave enough freedom for the reconstructed density to float around the prior: voids tend to be filled, and high density peaks are not saturated. On the contrary, a large value for σ_γ allows significant deviations from the prior but makes the iteration procedure less stable. For this reason, the reconstruction is carried out in two steps. We first take a small value for $\sigma_\gamma = 0.0175$, and reconstruct the density while using equation (34) to determine accurately the most likely velocity. Because of our choice of σ_γ , the reconstructed density is not as contrasted as it should be, but this does not affect significantly the corresponding most likely velocity: it just makes it smoother. In the second step, we *fix* the most likely velocity at the value obtained from the first step. Thus equation (34) is disregarded, and we iterate once more on the density with a larger value of σ_γ , $\sigma_\gamma = 0.2$, allowing more variations of the density around the new prior – the reconstructed density obtained from the first step. The fact that the most likely velocity is fixed indeed makes the inversion more stable and allows larger values of σ_γ .

Fig. 8 illustrates how the method performs on two unsaturated LOSs: the first isolated and the latter nearby a cluster. The simulated spectra assume $A = 0.39$, $\beta = 0.4$, $\bar{T} = 10^4$ K, and were calculated after smoothing the density and velocity fields with a cube of size ~ 200 kpc (2 cells). The errors in the data are modelled as described in Section 5.2.2 with $(S/N, \sigma_0) = (100, 0.05)$ in equation (29). As expected, the reconstructed velocity matches the original only when there is no significant structure close to the LOS, likely to induce large-scale infall contamination. The bottom panels of Fig. 7 show that the reconstructed density reproduces well the shape of most structures, except that they are not correctly located along the velocity axis in the bottom right panel.

Note that our two-step procedure is similar in spirit to that proposed by Nusser & Haehnelt (1999a), although we use same smoothing length ξ_x in both steps, which allows more small-scale features on the reconstructed density. Also, our method is not yet able to deal with spectra containing significantly saturated absorption lines: in that case, the inversion is much less stable and the reconstructed most likely velocity is often unrealistic, even if the LOS is isolated. Finally, we assumed that the kernel function $K^{(v)}(x, y)$ was known, which should not

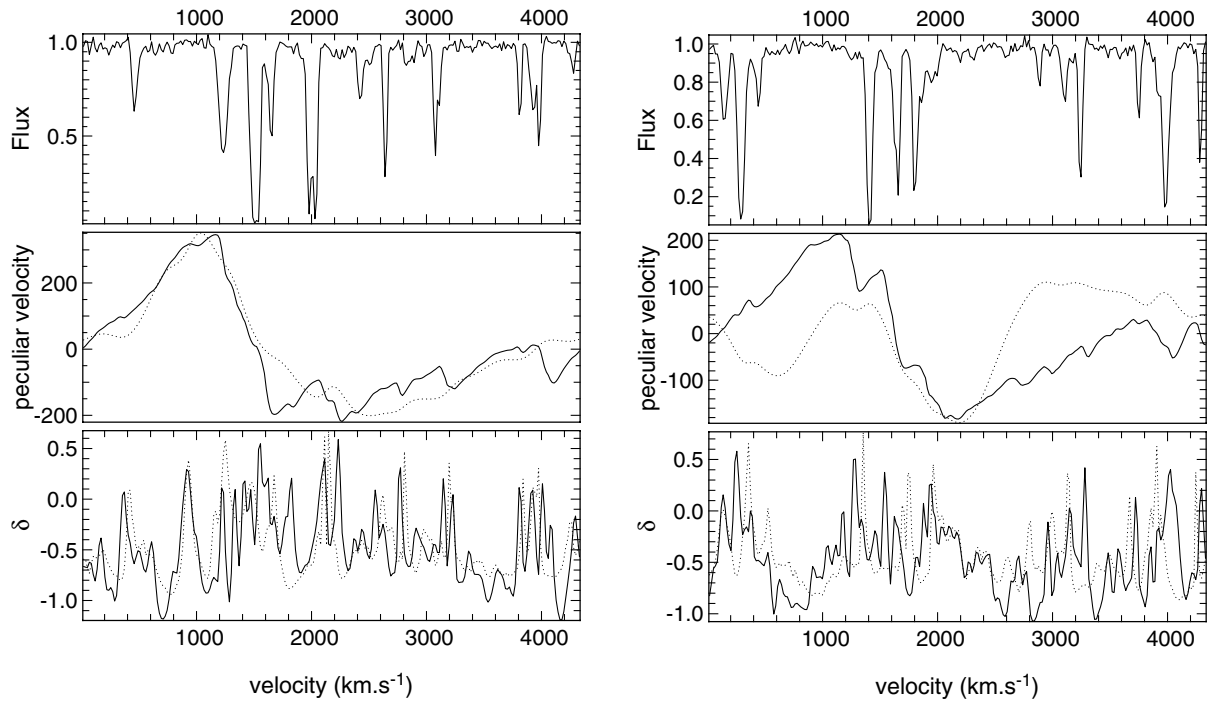


Figure 8. Inversion while accounting for peculiar velocity with strong prior. Simulation S is used to test the method. Two examples are considered, according to whether there is a large structure near the LOS or not (respectively right and left panels). *Top panels:* the simulated spectra. *Middle panels:* the simulated (solid line) and most likely (dotted line) peculiar velocity along the LOS. *Bottom panels:* the simulation (solid line) and reconstructed (dotted line) log-density (in \log_{10} units).

be the case in reality: a more detailed study of the effects of the assumed shape for this function will be needed in the future to fully qualify the method.

5.4.3 Floating prior for the velocities

A less biased representation of the underlying field would be to assume that γ and v_p are two fields which are statistically correlated (by the dynamics) but whose realizations are independent. The model is formally identical to equation (33), with the restriction that v_p does *not* obey equation (34) anymore. The vector of the model parameters is: $\mathbf{M} = [\gamma(x), v_p(x)]$. The correlation between γ and v_p , $\mathbf{C}_{v\gamma}$ is considered to be linear. Recall that the prior variance–covariance matrix, \mathbf{C}_0 , has three independent terms, shown in the bottom right panel of Fig. 6:

$$\mathbf{C}_0 = \begin{pmatrix} \mathbf{C}_{\gamma\gamma} & \mathbf{C}_{v\gamma} \\ \mathbf{C}_{v\gamma}^\top & \mathbf{C}_{vv} \end{pmatrix}. \quad (35)$$

The penalty function then obeys equation (22), and realizations of the velocity field are entitled to float around their most likely values, equation (14). The corresponding model, g , is sketched in Appendix D2.2. The iterative procedure presented in Appendix A brings the reduced χ^2 down from values of about a 100 to $1 \pm \sqrt{2/N}$ in a few iterations, but does not converge if peculiar velocities induce displacements larger than the effective width of the absorption lines. Even though the weak prior inversion is more elegant and easier to implement than the strong prior approach (cf. Appendix D2.2), it seems to fail to constrain sufficiently our model when redshift distortion is important. This arises because the effective correlation in equation (22) is too weak to induce convergence.

5.4.4 Discussion

A priori, the best approach for reconstructing the density in redshift space would be to use the explicit Bayesian method with a floating prior for the velocity described in Section 5.4.3. However, our preliminary analyses show that this method fails to converge when applied to *one* LOS if redshift distortion becomes of the order of the width of absorption lines, which is unfortunately the case in realistic situations. The strong prior inversion of Section 5.4.2, tested again on one LOS, seems to be more reliable, but gives accurate reconstruction only if the considered LOS is unsaturated and is isolated from large structures. The only reliable way to improve the reconstruction is therefore to have more information on the 3D structure of the IGM through bundles of LOSs, as studied in Section 5.4.1. The difference between Sections 5.4.3 and 5.4.2 would then vanish, since the discrepancy between the most likely velocity and the actual field becomes smaller and smaller, while the correlation between the density and the velocity becomes simultaneously tighter and tighter. However, we have not explicitly tested the methods of Sections 5.4.2 and 5.4.3 on several LOSs: this is left for future work.

6 CONCLUSIONS

In this paper an explicit Bayesian technique and a constrained mean field method have been proposed to recover various properties of the intergalactic medium from observations of the Lyman α forest along LOSs to quasars. In particular, our preliminary analyses suggest that these methods may be used (i) to recover the large-scale 3D topology of the IGM from inversion of a network of adjacent LOSs observed at low spectral resolution, (ii) to constrain the physical characteristics of the gas from inversion of single LOSs observed at high spectral resolution, (iii) to investigate how the number of, and the distance between, LOSs constrain the projected peculiar velocities, and (iv) to correct in part for redshift distortions induced by these velocities using either strong or weak priors.

Both approaches rely on prior assumptions on the covariance of the log-density field and the cross-correlation between the log-density field and the peculiar velocity field.

These methods are used in various régimes: as extrapolation tools to recover the 3D structure of the IGM, as non-linear deconvolution tools to correct for blending, as non-parametric field extractors, and as model fitting routines to constrain the parameters of the equation of state.

We have demonstrated (Section 3.3) that as far as extrapolation is concerned the standard constrained mean field interpolation scheme could be viewed as a specific linear subcase of the Bayesian inversion scheme presented in Section 3.1. The method presented in Section 3.1 is therefore complementary to, and more general than, standard constrained mean field techniques: it can also cope with thermal broadening and finite S/N, in a manner similar to Wiener filtering, but allows for non-linear models and non-zero mean priors. The correlation functions required for the prior need not be measured in the simulations, and can be postulated. It is more flexible, since some level of redshift distortion can in principle be corrected for using the full 3D information along the bundle (although we did not demonstrate it explicitly in this paper). It is well suited for this kind of problems, since it deals directly with unknown continuous fields (i.e., the parameter space is the Hilbert space L_2 ; see, e.g. equation D16). In contrast with the Lucy–Richardson algorithm, regularization is built in.

We have shown that temperature inversion is degenerate with respect to two parameters describing the equation of state of the gas, the temperature scalefactor \bar{T} and the effective polytropic index β .

Recall that we have assumed in this paper the correlation matrices of the log density to be fixed a priori, together with the cross-correlation of the log density and the velocities when dealing with peculiar velocities. When the method is applied to real data, we will proceed iteratively and recompute these (cross-)correlations once the 3D reconstruction is achieved. We expect this procedure to converge, and that the convergence limit will not depend too strongly on the initial prior.

A thorough analysis of the various biases involved in the methods presented here is postponed to a companion paper, which will investigate statistically the properties of the reconstructed fields and the degeneracies involved in recovering the density and the temperature, while relying on numerical hydrodynamical simulations. Since this inversion method relies on existing cross-correlation between the density and the velocity fields, it should still be applicable on scales where dark matter dynamics is less relevant, so long as such correlations exist. We have left aside for now the simultaneous true 3D deconvolution of both the temperature and the peculiar velocities.

ACKNOWLEDGMENTS

We thank F. Bernardeau, E. Thiébaud and D. Pogosyan for many discussions and an introduction to constrained mean field theory. JLV and PP also thank Bob Carswell for useful discussions. JLV was supported in part by the EC TMR network ‘Galaxy Formation and Evolution’ and the Centre de Données Astronomiques de Strasbourg. This work was supported by the Programme National de Cosmologie.

REFERENCES

- Abel T., Haehnelt M., 1999, *ApJ*, 520, L13
- Adler R. J., 1981, *The Geometry of Random Fields*. Wiley, Chichester
- Alimi J.-M., Bouchet F. R., Pellat R., Sygnet J.-F., Moutarde F., 1990, *ApJ*, 354, 3
- Backus G., Gilbert F., 1970, *Phil. Trans. R. Soc. London*, 266, 123
- Bardeen J. M., Bond J. R., Kaiser N., Szalay A. S., 1986, *ApJ*, 304, 15
- Bertschinger E., 1995, *A&AS*, 186, 2602
- Bi HongGuang, Davidsen A. F., 1997, *ApJ*, 477, 579
- Bond J. R., Wadsley J. W., 1998, in Petitjean P., Charlot S. eds, *Proc. 13th IAP meeting, Structure et Evolution du Milieu Inter-Galactique Revele par Raies D’Absorption dans le Spectre des Quasars*. Editions Frontières, Paris, p. 143
- Bouchet F. R., Adam J.-C., Pellat R., 1985, *A&A*, 144, 413
- Boulade O. et al., 1998, in D’Odorico S. ed., *Optical Astronomical Instrumentation*. Proc. SPIE 3355, p. 614
- Cen R., Miralda-Escudé J., Ostriker J. P., Rauch M., 1994, *ApJ*, 437, L9
- Colombi S., 1996, in Ansari, Giraud-Héraud, Trân Thanh Vân eds, *Dark Matter in Cosmology, Quantum Measurements, Experimental Gravitation*, Proc. of the XXXIst Rencontres de Moriond. Editions Frontières, Gif-sur-Yvette, France, p. 199
- Colombi S., Bouchet F. R., Schaeffer R., 1994, *A&A*, 281, 301
- Craig I. J. D., Brown J. C., 1986, *Inverse Problems in Astronomy*. Adam Hilger Ltd., Bristol and Boston
- Croft R. A. C., Weinberg D. H., Katz N., Hernquist L., 1998, *ApJ*, 495, 44
- Croft R. A. C., Weinberg D. H., Pettini M., Hernquist L., Katz N., 1999, *ApJ*, 520, 1
- Crotts A. P. S., Fang Y., 1998, *ApJ*, 502, 16

- Dinshaw N. et al., 1995, *Nat*, 373, 223
D’Odorico V. et al., 1998, *A&A*, 339, 678
Folkes S. et al., 1999, *MNRAS*, 308, 459
Gnedin N., Hui L., 1998, *MNRAS*, 296, 44
Hamilton A. J. S., Kumar P., Lu E., Matthews A., 1991, *ApJ*, 374, L1
Hernquist L., Katz N., Weinberg D. H., Miralda-Escudé J., 1996, *ApJ*, 457, L51
Hivon E., 1995, PhD thesis Université Paris XI
Hockney R. W., Eastwood J. W., 1981, *Computer Simulation Using Particles*. McGraw Hill, New York
Hoffman Y., Ribak E., 1992, *ApJ*, 384, 448
Hui L., 1999, *ApJ*, 516, 519
Hui L., Gnedin N. Y., 1997, *MNRAS*, 292, 27
Hui L., Rutledge R. E., 1999, *ApJ*, 517, 541
Hui L., Gnedin N. Y., Zhang Y., 1997, *ApJ*, 486, 599
Hui L., Stebbins A., Burles S., 1999, *ApJ*, 511, L5
Impey C. D., Foltz C. B., Petry C. E., Browne I. W. A., Patnaik A. R., 1996, *ApJ*, 462, L53
Jenkins A. et al., 1998, *ApJ*, 499, 20
Le Fèvre O. et al., 1998, in Colombi S., Mellier Y., Rabban B. eds, *Proc. 14th IAP meeting. Wide Field Surveys in Cosmology*. Editions Frontières, Paris, p. 327
Longuet-Higgins M. S., 1957, *Phil. Trans. Roy. Soc. London A*, 249, 321
Lucy L., 1974, *AJ*, 79, 745
Meiksin A., Madau P., 1993, *ApJ*, 412, 34
Miralda-Escudé J., Cen R., Ostriker J. P., Rauch M., 1996, *ApJ*, 471, 582
Moutarde F., Alimi J.-M., Bouchet F. R., Pellat R., Ramani A., 1991, *ApJ*, 382, 377
Mückel J. P., Petitjean P., Kates R., Riediger R., 1996, *A&A*, 308, 17
Nusser A., Haehnelt M., 1999a, *MNRAS*, 303, 179
Nusser A., Haehnelt M., 1999b, *astro-ph/9906406*
Peacock J. A., Dodds S. J., 1996, *MNRAS*, 280, 19, P
Peebles P. J. E., 1980, *The Large-Scale Structure of the Universe*. Princeton Univ. Press, Princeton, p. 153
Petitjean P. et al., 1993, *MNRAS*, 262, 499
Petitjean P., Mückel J., Kates R. E., 1995, *A&A*, 295, L9
Petitjean P., Surdej J., Smette A., Shaver P., Mückel J., Remy M., 1998, *A&A*, 334, L45
Pichon C., Thiébaud E., 1998, *MNRAS*, 301, 419
Press W. H., Rybicki G. B., 1993, *APJ*, 418, 585
Rahman A., 1964, *Phys. Rev. A*, 136, 405
Rauch M., Haehnelt M., 1995, *MNRAS*, 275, 76
Rauch M. et al., 1997, *ApJ*, 489, 7
Reisenegger A., Miralda-Escudé J., 1995, *ApJ*, 449, 476
Rice S. O., 1944, *Bell System Tech J.*, 23, 282
Rice S. O., 1945, *Bell System Tech J.*, 24, 41
Ricotti M., Gnedin N., Shull J. M., 2000, *ApJ*, 534, 41
Schaye J., Theuns T., Leonard A., Efstathiou G., 1999, *MNRAS*, 310, 57
Scoccimarro R., 1998, *MNRAS*, 299, 1097
Smette A. et al., 1995, *A&AS*, 113, 199
Szalay A., 2000, *Proc. IAU Symp. 204, The Extragalactic Infrared Background and its Cosmological Implications*. Astron. Soc. Pac., San Francisco, p. 16
Tarantola A., Valette B., 1982a, *J. Geophys.*, 50, 159
Tarantola A., Valette B., 1982b, *Reviews of Geophysics and Space Physics*, 20, 219
Theuns T., Leonard A., Schaye J., Efstathiou G., 1999, *MNRAS*, 303, L58
Theuns T., Schaye J., Haehnelt M., 2000, *MNRAS*, 315, 600
Valageas P., Schaeffer R., Silk J., 1999, *A&A*, 345, 691
Vergely J. L., Freire Ferrero R., Siebert A., Valette B., 2001, *A&A*, 366, 1016
Weinberg D. H., 1999, in Banday A. J., Sheth R. K., da Costa L. N. eds, *Proc. of ESO/MPA conf. Evolution of Large Scale Structure: from Recombination to Garching*. ESO, Garching, p. 346
Weinberg D. H., Croft R. A. C., Hernquist L., Katz N., Pettini M., 1999, *ApJ*, 522, 563
Wiener N., 1949, *Extrapolation and Smoothing of Stationary Time Series*. Wiley, New York
Zaroubi S., Hoffman Y., Fisher K. B., Lahav O., 1995, *ApJ*, 449, 446
Zel’dovich Ya. B., 1970, *A&A*, 5, 84
Zhang Yu., Anninos P., Norman M. L., 1995, *ApJ*, 453, L57

APPENDIX A: MINIMIZATION PROCEDURE

In this section we sketch an iterative procedure leading to the optimization of the posterior probability of the model for a given data set in equation (10). The minimum of the argument of the exponential in equation (10) is shown by a simple variational argument (Tarantola & Valette, 1982a,b) to obey the implicit equation

$$\langle \mathbf{M} \rangle = \mathbf{M}_0 + \mathbf{C}_0 \cdot \mathbf{G}^\perp \cdot (\mathbf{C}_d + \mathbf{G} \cdot \mathbf{C}_0 \cdot \mathbf{G}^\perp)^{-1} \cdot [\mathbf{D} + \mathbf{G} \cdot (\langle \mathbf{M} \rangle - \mathbf{M}_0) - g(\langle \mathbf{M} \rangle)], \quad (\text{A1})$$

with \mathbf{G} , the matrix of partial derivatives:

$$\mathbf{G} = \left(\frac{\partial g}{\partial \mathbf{M}} \right). \quad (\text{A2})$$

This minimum is found using an iterative procedure:

$$\mathbf{M}_{[k+1]} = \mathbf{M}_0 + \mathbf{C}_0 \cdot \mathbf{G}_{[k]}^\perp \cdot (\mathbf{C}_d + \mathbf{G}_{[k]} \cdot \mathbf{C}_0 \cdot \mathbf{G}_{[k]}^\perp)^{-1} \cdot [\mathbf{D} + \mathbf{G}_{[k]} \cdot (\mathbf{M}_{[k]} - \mathbf{M}_0) - g(\mathbf{M}_{[k]}], \quad (\text{A3})$$

where subscript $[k]$ refers to the iteration order. In this scheme the minimum corresponds to $\tilde{\mathbf{M}} = \mathbf{M}_{[\infty]}$, and in practice is found via a convergence criterion on the relative changes between iteration $[k]$ and $[k+1]$. For the sake of numerical efficiency, rather than inverting $(\mathbf{C}_d + \mathbf{G}_{[k]} \cdot \mathbf{C}_0 \cdot \mathbf{G}_{[k]}^\perp)$, we solve for the vector $\mathbf{W}_{[k]}$ satisfying

$$\mathbf{S}_{[k]} \cdot \mathbf{W}_{[k]} = [\mathbf{D} + \mathbf{G}_{[k]} \cdot (\mathbf{M}_{[k]} - \mathbf{M}_0) - g(\mathbf{M}_{[k]})], \quad \text{where} \quad \mathbf{S}_{[k]} = \mathbf{C}_d + \mathbf{G}_{[k]} \cdot \mathbf{C}_0 \cdot \mathbf{G}_{[k]}^\perp, \quad (\text{A4})$$

and iterate:

$$\mathbf{M}_{[k+1]} = \mathbf{M}_0 + \mathbf{C}_0 \cdot \mathbf{G}_{[k]}^\perp \cdot \mathbf{W}_{[k]}. \quad (\text{A5})$$

From now on, we drop the subscript $[k]$. Once the maximum of equation (10) has been reached, an approximation of the internal error made on the parameter estimation is derived from a second-order development of the posterior distribution function in the vicinity of the solution:

$$\mathbf{C}_M = \mathbf{C}_0 - \mathbf{C}_0 \cdot \mathbf{G}^\perp \cdot \mathbf{S}^{-1} \cdot \mathbf{G} \cdot \mathbf{C}_0. \quad (\text{A6})$$

The high spatial frequency fluctuations are lost in the inverse process because of limited resolution and finite S/N. The *prior* correlation function therefore plays an important role to transform an ill-posed problem into an invertible one. How is the density information degraded in the spectra? This question can be addressed via the resolving kernel, \mathbf{R} , introduced for the first time by Backus & Gilbert (1970) and which gives the spread of the density estimation at a given position. Suppose that we know the true model, \mathbf{M}_{true} . The data can be written: $\mathbf{D} = g(\mathbf{M}_{\text{true}})$. Approximating locally operator g near its minimum as a linear operator, equation (A1) yields:

$$\langle \mathbf{M} \rangle - \mathbf{M}_0 = \mathbf{C}_0 \cdot \mathbf{G}^\perp \cdot \mathbf{S}^{-1} \cdot \mathbf{G} \cdot (\mathbf{M}_{\text{true}} - \mathbf{M}_0) \equiv \mathbf{R} \cdot (\mathbf{M}_{\text{true}} - \mathbf{M}_0), \quad (\text{A7})$$

which defines the resolving kernel $\mathbf{R}(x, x')$ as a low-bandpass filter.

APPENDIX B: CONSTRAINTS, MEAN FIELDS AND MULTIPLE LINE OF SIGHTS

As a thought experiment, let us assume that we know the density contrast δ on n points and ask what the corresponding most likely velocity (or density) at points labelled $k = 1 \dots p$, ϖ_k is. We shall not assume that the densities $\delta_1, \dots, \delta_n$ are necessarily along the same LOS, nor that the quantity ϖ_k is sought along any of these. Let $X = [\varpi_1, \dots, \varpi_p, \delta_1, \dots, \delta_n]$. We define

$$\mathbf{C} \equiv \begin{bmatrix} \langle \varpi_1 \varpi_1 \rangle & \dots & \langle \varpi_1 \varpi_p \rangle & \langle \varpi_1 \delta_1 \rangle & \dots & \langle \varpi_1 \delta_n \rangle \\ \vdots & & \ddots & \vdots & & \vdots \\ \langle \varpi_1 \varpi_p \rangle & \dots & \langle \varpi_p \varpi_p \rangle & \langle \varpi_p \delta_1 \rangle & \dots & \langle \varpi_p \delta_n \rangle \\ \langle \varpi_1 \delta_1 \rangle & \dots & \langle \varpi_p \delta_1 \rangle & \langle \delta_1 \delta_1 \rangle & \dots & \langle \delta_1 \delta_n \rangle \\ \vdots & & \ddots & \vdots & & \vdots \\ \langle \varpi_1 \delta_n \rangle & \dots & \langle \varpi_p \delta_n \rangle & \langle \delta_1 \delta_n \rangle & \dots & \langle \delta_n \delta_n \rangle \end{bmatrix} \equiv \begin{bmatrix} \mathbf{C}_{ww} & \mathbf{C}_{w\delta} \\ \mathbf{C}_{w\delta}^\perp & \mathbf{C}_{\delta\delta} \end{bmatrix}, \quad (\text{B1})$$

so that \mathbf{C}_{ww} is the $p \times p$ autocorrelation matrix of the sought field, $\mathbf{C}_{\delta\delta}$ is the $n \times n$ autocorrelation matrix of the known density field, and $\mathbf{C}_{w\delta}$ is the $p \times n$ cross-correlation matrix of the sought field with the density field. The joint probability of achieving velocity ϖ_k and density profile $\delta_1, \dots, \delta_n$ is given by

$$p(X) d^{n+p} X = p(\varpi_1, \dots, \varpi_p, \delta_1, \dots, \delta_n) d\varpi_1 \dots d\varpi_p d\delta_1 \dots d\delta_n = \exp \left\{ -\frac{1}{2} \left[\sum_{a,b=1 \dots n+p} (C^{-1})_{a,b} X_a X_b \right] \right\} \frac{d^{n+p} X}{\sqrt{(2\pi)^{n+p} \det |C|}}.$$

The argument of the exponential can be rearranged as

$$(\varpi, \delta)^\perp \cdot \begin{bmatrix} \mathbf{C}_{ww} & \mathbf{C}_{w\delta} \\ \mathbf{C}_{w\delta}^\perp & \mathbf{C}_{\delta\delta} \end{bmatrix}^{-1} \cdot (\varpi, \delta) = (\varpi - \mathbf{C}_{w\delta} \cdot \mathbf{C}_{\delta\delta}^{-1} \cdot \delta)^\perp \cdot (\mathbf{C}_{ww} - \mathbf{C}_{w\delta} \cdot \mathbf{C}_{\delta\delta}^{-1} \cdot \mathbf{C}_{w\delta}^\perp)^{-1} \cdot (\varpi - \mathbf{C}_{w\delta} \cdot \mathbf{C}_{\delta\delta}^{-1} \cdot \delta) + \text{rest} \quad (\text{B2})$$

where ‘rest’ stands for terms independent of $\varpi \equiv (\varpi_1 \dots \varpi_p)$. Applying Bayes’s theorem, the conditional probability of ϖ , given the density

profile $(\delta_1, \dots, \delta_n)$, obeys

$$p(\varpi_1, \dots, \varpi_p | \delta_1, \dots, \delta_n) d\varpi_1 \dots d\varpi_p = p(\varpi_1, \dots, \varpi_p, \delta_1, \dots, \delta_n) / p(\delta_1, \dots, \delta_n) d\varpi_1 \dots d\varpi_p,$$

which in turns implies that

$$p(\varpi_1, \dots, \varpi_p | \delta_1, \dots, \delta_n) \propto \exp \left[-\frac{1}{2} \{ (\varpi - \mathbf{C}_{w\delta} \cdot \mathbf{C}_{\delta\delta}^{-1} \cdot \delta)^\perp \cdot (\mathbf{C}_{ww} - \mathbf{C}_{w\delta} \cdot \mathbf{C}_{\delta\delta}^{-1} \cdot \mathbf{C}_{w\delta}^\perp)^{-1} \cdot (\varpi - \mathbf{C}_{w\delta} \cdot \mathbf{C}_{\delta\delta}^{-1} \cdot \delta) \} \right],$$

since $p(\delta_1, \dots, \delta_n)$ is independent of ϖ . The maximum of the conditional probability is therefore reached for $\langle \varpi \rangle$ given by

$$\langle \varpi \rangle = \mathbf{C}_{w\delta} \cdot \mathbf{C}_{\delta\delta}^{-1} \cdot \delta. \quad (\text{B3})$$

Appendix B1 Peculiar velocity–density relation

Let us now be more specific about ϖ_k and assume, in this subsection, that we are seeking the most likely peculiar velocity field, v_k , where we dropped the subscript p referring to ‘peculiar’.

Appendix B1.1 One line of sight

Recall that nothing has been said about the relative position of the δ_i and the v_k at this stage. Let us now assume for a while that the subscript i refers to a regular ordering along the LOS, so that $\delta_i = \delta(i\Delta x)$, and $v_i = v(i\Delta x)$. Let us also introduce the intermediate field, $\mathbf{u} = (u_i)_{i=1\dots n} \equiv \mathbf{C}_{\delta\delta}^{-1} \cdot \delta$, so that equation (B3) reads

$$\langle \mathbf{v} \rangle = \mathbf{C}_{v\delta} \cdot \mathbf{u}, \quad \delta = \mathbf{C}_{\delta\delta} \cdot \mathbf{u}. \quad (\text{B4})$$

Multiplying both sides of equation (B4) by Δx , we get

$$\begin{aligned} \sum_j (C_{v\delta})_{ij} u_j \Delta x &= \sum_j u [j\Delta x] \langle v[j\Delta x] \delta[(i-j)\Delta x] \rangle \Delta x = \langle v[i\Delta x] \rangle \Delta x, \\ \sum_j (C_{\delta\delta})_{ij} u_j \Delta x &= \sum_j u [j\Delta x] \langle \delta[j\Delta x] \delta[(i-j)\Delta x] \rangle \Delta x = \delta[i\Delta x] \Delta x. \end{aligned} \quad (\text{B5})$$

In the limit of Δx going to zero, equation (B5) reads

$$\int \langle \delta(x - x') v(x') \rangle u(x') dx' = \langle v(x) \rangle \Delta x \quad \text{and} \quad \int \langle \delta(x - x') \delta(x') \rangle u(x') dx' = \delta(x) \Delta x. \quad (\text{B6})$$

Transforming equation (B6) in Fourier space leads to

$$\langle \tilde{v} \rangle(k_x) = \frac{P_{v\delta,1D}(k_x)}{P_{\delta\delta,1D}(k_x)} \tilde{\delta}(k_x), \quad (\text{B7})$$

where $P_{\delta\delta,1D}(k_x)$ and $P_{v\delta,1D}(k_x)$ are respectively the 1D density power spectrum and the 1D mixed velocity density power spectrum, while $\tilde{\delta}(k_x)$ and $\langle \tilde{v} \rangle(k_x)$ are the Fourier transform of $\delta(x)$ and $\langle v \rangle(x)$ respectively. Here the 1D power spectra satisfy

$$P_{\delta\delta,1D}(k_x) = \int P_{3D}(\mathbf{k}) W_J(\mathbf{k}) d^2 k_\perp \quad \text{and} \quad P_{v\delta,1D}(k_x) = \int \frac{P_{3D}(\mathbf{k}) k_x}{k_x^2 + k_\perp^2} W_J(\mathbf{k}) d^2 k_\perp, \quad (\text{B8})$$

where $P_{3D}(\mathbf{k})$ is the 3D power spectrum of the density contrast, while $W_J(\mathbf{k})$ is a window function whose characteristic scale R_J should be the Jeans length, but is chosen here to be the maximum of the Jeans length and the sampling scale. Indeed, below this latter scale no information is to be derived from the data. Note that the direct inversion of equation (B3) may lead to significant aliasing if the power spectrum has energy beyond the cut-off frequency $1/R_J$. The power spectrum ratio in equation (B7) is an antisymmetric filter which relates the most likely velocity field to a given density field in linear theory.

Equation (B7) can be transformed back into real space as

$$\langle v \rangle(x) = \int K^{(v)}(x, x') \delta(x') dx', \quad \text{where} \quad K^{(v)}(x, x') \equiv \frac{1}{2\pi} \int e^{ik_x(x-x')} \frac{P_{v\delta,1D}(k_x)}{P_{\delta\delta,1D}(k_x)} dk_x. \quad (\text{B9})$$

This filter is illustrated in Fig. 6. Equation (B9) could be used to derive $K^{(v)}(x, x')$ from perturbation theory in the weakly non-linear régime given an initial power spectrum. In practice, this filter is constructed here from the simulation in the following manner: for each LOS in the

simulation, we compute the FFT of the overdensity and of the velocity; we multiply one by the complex conjugate of the other, and repeat the operation on the whole box; we then average over the box (using a bundle of 60×60 LOSs) and FFT-transform back in real space: this yields equation (B9).

Appendix B1.2 Multiple lines of sight

Let us now turn to the more general problem of multiple LOSs. How can we take advantage of larger scale information on multiple LOSs to constrain the velocity *along* the measured LOSs ?

To conduct the calculation which follows, we order the $\delta_1, \dots, \delta_n$, where $n = Lp$, so that the first p corresponds to the first LOS, the next p to the second LOS, and so on for the $\ell = 1 \dots L$ LOSs. Our purpose here is to account for the fact that in realistic situations, the LOSs distribution on the sky is not necessarily uniform and that the volume covered by all LOSs is rather elongated (i.e., $L \ll p$). For the sake of numerical efficiency, we Fourier-transform along the longitudinal direction and are left with a matrix representation for the two transverse dimensions. We write each block in Fourier space in terms of the corresponding 1D power spectra (this is possible since both Fourier transform and matrix multiplication are linear operations, which therefore commute when applied on different directions); following the derivation of equation (B7) we find

$$\langle \tilde{\mathbf{v}} \rangle = \tilde{\Xi} \cdot \tilde{\Delta}^{-1} \cdot \tilde{\delta}, \quad (\text{B10})$$

where

$$\tilde{\Delta} \equiv \begin{bmatrix} P_{\delta\delta}^{11}(k_x) & \dots & P_{\delta\delta}^{1L}(k_x) \\ \vdots & \ddots & \vdots \\ P_{\delta\delta}^{L1}(k_x) & \dots & P_{\delta\delta}^{LL}(k_x) \end{bmatrix}, \quad \tilde{\Xi} \equiv \begin{bmatrix} P_{v\delta}^{11}(k_x) & \dots & P_{v\delta}^{1L}(k_x) \\ \vdots & \ddots & \vdots \\ P_{v\delta}^{L1}(k_x) & \dots & P_{v\delta}^{LL}(k_x) \end{bmatrix}, \quad (\text{B11})$$

and $\langle \tilde{\mathbf{v}} \rangle = [\tilde{v}^1(k_x), \dots, \tilde{v}^L(k_x)]$, $\tilde{\delta} = [\tilde{\delta}^1(k_x), \dots, \tilde{\delta}^L(k_x)]$, where the superscript refers to the L LOSs. Here

$$P_{\delta\delta}^{\ell\ell'}(k_x) = \int \exp(i\mathbf{k}_\perp \cdot \{\mathbf{x}_{\perp,\ell} - \mathbf{x}_{\perp,\ell'}\}) P_{3D}(\mathbf{k}) W_{J,\tilde{R}}(\mathbf{k}) d^2\mathbf{k}_\perp, \quad (\text{B12})$$

$$P_{v\delta}^{\ell\ell'}(k_x) = \int \exp(i\mathbf{k}_\perp \cdot \{\mathbf{x}_{\perp,\ell} - \mathbf{x}_{\perp,\ell'}\}) W_{J,\tilde{R}}(\mathbf{k}) \frac{P_{3D}(\mathbf{k}) k_x}{k_x^2 + \mathbf{k}_\perp^2} d^2\mathbf{k}_\perp. \quad (\text{B13})$$

The window function, $W_{J,\tilde{R}}(k_x, \mathbf{k}_\perp)$ involves two scales: the longitudinal Jeans length and the transverse mean inter-LOS separation, \tilde{R} . The latter filtering is required to apodize the inversion. Note that $P_{\delta\delta}^{\ell\ell}(k_x) = P_{\delta\delta,1D}(k_x)$ and $P_{v\delta}^{\ell\ell}(k_x) = P_{v\delta,1D}(k_x)$ are given by equation (B8). Equation (B10) reads back into real space:

$$v_{\ell'}(x) = \sum_{\ell} \int K_{\ell'\ell}(x, x') \delta_{\ell}(x') dx', \quad \text{where} \quad K_{\ell'\ell}(x, x') \equiv \frac{1}{2\pi} \int e^{ik_x(x-x')} (\tilde{\Xi} \cdot \tilde{\Delta}^{-1})_{\ell'\ell} dk_x, \quad (\text{B14})$$

where the matrix $\tilde{\Xi} \cdot \tilde{\Delta}^{-1}$ is given in equation (B11). In practice, this filter is also constructed here from the simulation following the prescription sketched above: for each bundle of LOSs in the simulation, we compute the FFT of the log density and of the velocity; we multiply one bundle by the complex conjugate of the other, and repeat the operation on the whole box; we then average over the box (using a bundle of 20×20 LOSs): this yields the matrix (B11). The matrix multiplication in equation (B14) is carried Fourier mode by Fourier mode, while the inverse Fourier transform is done by FFT.

Appendix B2 3D density-LOSs density relation

Let us now assume that $\tilde{\mathbf{w}}_k$ refers to the 3D density on a grid of P points at the point $\mathbf{x}_\lambda = (\mathbf{x}_{\perp,\lambda}, x_\lambda)_{\lambda=1\dots P}$. No restriction on the location of \mathbf{x}_λ along the LOSs applies here. Under these assumptions, the above section translate as:

$$\langle \delta^{(3D)} \rangle(\mathbf{x}_\lambda) = \sum_{\ell} \int K_{\lambda\ell}^{(3D)}(\mathbf{x}_\lambda, \mathbf{x}'_\ell) \delta_{\ell}(x'_\ell) dx'_\ell, \quad \text{where} \quad K_{\lambda\ell}^{(3D)}(\mathbf{x}_\lambda, \mathbf{x}'_\ell) \equiv \frac{1}{(2\pi)^3} \int \exp[i\mathbf{k} \cdot (\mathbf{x}_\lambda - \mathbf{x}'_\ell)] (\tilde{\Xi}_{3D} \cdot \tilde{\Delta}^{-1})_{\lambda\ell} d^3\mathbf{k} \quad (\text{B15})$$

with $\tilde{\Delta}$ obeying equation (B11) and

$$\tilde{\Xi}_{3D} = \begin{bmatrix} P_{3D}^{11}(k_x) & \dots & P_{3D}^{L1}(k_x) \\ \vdots & \ddots & \vdots \\ P_{3D}^{1P}(k_x) & \dots & P_{3D}^{LP}(k_x) \end{bmatrix}, \quad \text{given} \quad P_{3D}^{\ell\lambda}(k_x) = \int \exp(i\mathbf{k}_\perp \cdot \{\mathbf{x}_{\perp,\ell} - \mathbf{x}_{\perp,\lambda}\}) P_{3D}(\mathbf{k}) W_{J,\tilde{R}}(\mathbf{k}) d^2\mathbf{k}_\perp. \quad (\text{B16})$$

We check that when we consider a point on the LOSs, $\mathbf{x} = (\mathbf{x}_{\perp,\ell}, x)$, $K_{\lambda\ell}^{(3D)}(\mathbf{x}_\lambda, \mathbf{x}') = \delta_D(x - x') \tilde{\delta}_\ell^\lambda$, where $\tilde{\delta}_\ell^\lambda$ stands for the Kronecker symbol.

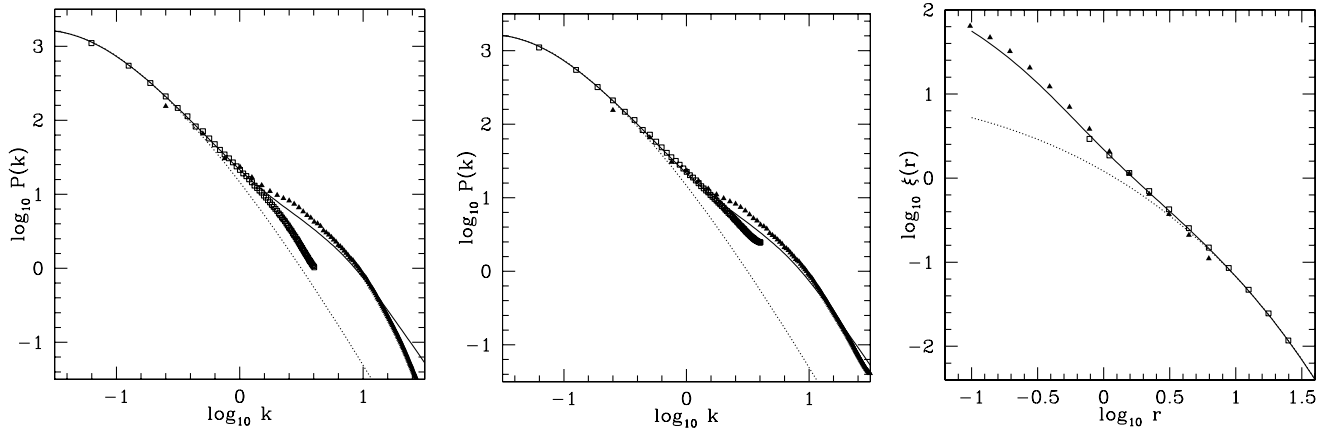


Figure C1. *Left-hand panel:* the power spectrum measured at $z = 2$ in the S (filled triangles) and B (open squares) simulations after adaptive smoothing, in logarithmic coordinates (wavenumber k is expressed in Mpc^{-1}). It is compared to linear theory (dots) and to non-linear Ansatz of Peacock & Dodds (1996, solid curve). *Middle panel:* same as left-hand panel, except that a correction for NGP damping was applied to the data prior to measurement of $P(k)$. *Right-hand panel:* the variance of the smoothed density field with a spherical cell of radius r is shown in logarithmic coordinates as a function of r , as explained in the text.

APPENDIX C: PROPERTIES OF THE SIMULATION

Note from Table 1 that the simulation boxes are rectangular. This long-box technique might be questionable. Indeed, the number of modes available in Fourier space is different along each coordinate axis. This anisotropic mode sampling contaminates the simulation, and the effect augments with the ratio between the largest and the smallest side of the box.

One way to test, at least partly, the quality of our N -body experiments is to compare second-order statistics measured in the simulations to theoretical predictions, as illustrated by Fig. C1. The left-hand panel shows the measured power spectrum, $P(k) = \langle |\delta_k|^2 \rangle$, in the density field smoothed with the procedure described in Section 4. Agreement with linear theory is appropriate at large scales, as expected. For comparison, we also plot the result obtained from the non-linear Ansatz of Hamilton et al. (1991) optimized for the power spectrum by Peacock & Dodds (1996). The overall agreement between measurements and non-linear theory is quite good, except at large values of k in both simulations. This is mainly the effect of the grid, and to a lesser extent a consequence of the adaptive Gaussian smoothing. Indeed, any procedure inferring on a grid a density from a particle distribution implies some smoothing with a window of approximately the mesh cell size. This induces large- k damping of the power spectrum. Here, the smoothing is not well defined, but most of the particles are in dense regions, due to non-linear clustering, and therefore the corresponding smoothing length, ℓ , is likely to be much smaller than the grid size. Thus, for most particles, all the contribution to the density is given to the nearest grid point (NGP). As a result, the Gaussian adaptive smoothing has a damping effect quite close, though slightly larger, to top-hat smoothing with a mesh cell (at least for sufficiently evolved stages). This is illustrated by middle panel of Fig. C1, which shows the power spectrum after correction for damping due to NGP assignment. Most of the missing power is recovered, as expected, and the agreement with theory is much improved. Note that the triangles tend to be slightly above the solid curve in the neighbourhood of $\log_{10} k \approx 0.4$. This irregularity is not surprising, given the small physical size of simulation S. It is probably associated with a rare event, for example an atypical cluster, although this does not show up significantly in Fig. 1.

The right-hand panel of Fig. C1 shows the real-space counterpart of the power spectrum. More precisely, it displays the variance of the smoothed density field with a sphere of radius ℓ as a function of ℓ . To measure it, we computed the density from the particle distribution on a grid twice thinner than the one used to do the simulation, using the cloud-in-cell method (CIC) (e.g. Hockney & Eastwood 1981). Then we corrected for CIC damping and smoothed with the top-hat window of size ℓ in Fourier space. Finally, back in real space, the variance of the density field was computed with the appropriate corrections for discreteness (e.g. Peebles 1980), i.e., $\sigma^2 = \langle \delta^2 \rangle - 1/\bar{N}$, where \bar{N} is the average particle count in a cell of radius ℓ . The scale range considered was $\lambda_g \leq \ell \leq L/4$, where L is the smallest dimension of the box and λ_g the spatial resolution of the simulation. As can be seen in Fig. C1, the agreement with theoretical predictions is quite good, even at $\ell \approx \lambda_g$, although the effect of softening of the forces is slightly felt at this point. Note also that the triangles are somewhat shifted up compared to the non-linear Ansatz (except at very large scales, where finite-volume-effect contamination reduces the value of σ^2 ; e.g. Colombi, Bouchet & Schaeffer 1994), as already noticed for the power spectrum.

APPENDIX D: IMPLEMENTATION OF THE INVERSE METHOD

Appendix D1 Neglecting peculiar velocities

Appendix D1.1 High-resolution spectra

When the spectral resolution is higher than 100 km^{-1} , thermal broadening cannot be neglected and our model reads

$$g_{ie}(\gamma) = A(\bar{z})c_1 \int \left(\int_{-\infty}^{+\infty} \{D_0(x, \mathbf{x}_\perp) \exp[\gamma(x, \mathbf{x}_\perp)]\}^{\alpha-\beta} \exp \left[-c_2 \frac{(w_{ie} - x)^2}{\{D_0(x, \mathbf{x}_\perp) \exp[\gamma(x, \mathbf{x}_\perp)]\}^{2\beta}} \right] dx \right) \delta_D(\mathbf{x}_\perp - \mathbf{x}_{\perp\ell}) d^2 \mathbf{x}_\perp, \quad (\text{D1})$$

where α , $A(\bar{z})$, c_1 , c_2 , β , $D_0(x, \mathbf{x}_\perp)$ and $w_{i\ell}$ are defined in equations (3)–(7) and equation (25). Since the model, $\mathbf{M} \equiv \gamma(x, \mathbf{x}_\perp)$ is a continuous field, we need to interpret equation (6) in terms of convolutions, and functional derivatives. In particular, the matrix of partial functional (Fréchet) derivatives, \mathbf{G} , has the following kernel:

$$(\mathbf{G})_{i\ell}(x, \mathbf{x}_\perp) \equiv \left(\frac{\partial g_{i\ell}}{\partial \gamma} \right)(x, \mathbf{x}_\perp) = A(\bar{z})c_1 D_0^{\alpha-\beta}(x, \mathbf{x}_\perp) \exp[(\alpha - \beta)\gamma(x, \mathbf{x}_\perp)] B_{i\ell}(x, \mathbf{x}_\perp) \delta_D(\mathbf{x}_\perp - \mathbf{x}_{\perp, \ell}), \quad (\text{D2})$$

with $\delta_D(\mathbf{x}_\perp - \mathbf{x}_{\perp, \ell})$ the Dirac delta function accounting for the singular distribution of LOSs, and

$$B_{i\ell}(x, \mathbf{x}_\perp) = \{(\alpha - \beta) + c_2 2\beta(w_{i\ell} - x)^2 D_0^{-2\beta}(x, \mathbf{x}_\perp) \exp[-2\beta\gamma(x, \mathbf{x}_\perp)]\} \mathcal{B}_{i\ell}(x, \mathbf{x}_\perp), \quad (\text{D3})$$

where

$$\mathcal{B}_{i\ell}(x, \mathbf{x}_\perp) = \exp \left[-c_2 \frac{(w_{i\ell} - x)^2}{\{D_0(x, \mathbf{x}_\perp) \exp[\gamma(x, \mathbf{x}_\perp)]\}^{2\beta}} \right]. \quad (\text{D4})$$

The operator, \mathbf{G} , defined by equation (D2) contracts over a given field, η , as:

$$(\mathbf{G})_{i\ell} \cdot \eta = \int A(\bar{z})c_1 D_0^{\alpha-\beta}(x, \mathbf{x}_\perp) \exp[(\alpha - \beta)\gamma(x, \mathbf{x}_\perp)] B_{i\ell}(x, \mathbf{x}_{\perp, \ell}) \eta(x, \mathbf{x}_{\perp, \ell}) dx. \quad (\text{D5})$$

Appendix D1.2 Low-resolution spectra

At low spectral resolution, the model spells

$$g_{i\ell}(\gamma) = A(\bar{z}) \iint \int (D_0(x, \mathbf{x}_\perp) \exp[\gamma(x, \mathbf{x}_\perp)])^\alpha \delta_D(x - w_{i\ell}) \delta_D(\mathbf{x}_\perp - \mathbf{x}_{\perp, \ell}) dx d^2 \mathbf{x}_\perp, \quad (\text{D6})$$

which corresponds to the limit $c_2 \rightarrow \infty$ in equation (D1). The kernel of partial functional derivatives \mathbf{G} obeys

$$(\mathbf{G})_{i\ell}(x, \mathbf{x}_\perp) = A(\bar{z})\alpha D_0^\alpha(x, \mathbf{x}_{\perp, \ell}) \exp[\alpha\gamma(x, \mathbf{x}_{\perp, \ell})] \delta_D(x - w) \delta_D(\mathbf{x}_\perp - \mathbf{x}_{\perp, \ell}). \quad (\text{D7})$$

For instance, $(\mathbf{G} \cdot \mathbf{C}_0 \cdot \mathbf{G}^\perp)_{i\ell, jm}$ in equation (A1) reads

$$A(\bar{z})^2 \alpha^2 C_{\gamma\gamma}(w_{i\ell}, w_{jm}, \mathbf{x}_{\perp, \ell}, \mathbf{x}_{\perp, m}) D_0^\alpha(w_{i\ell}, \mathbf{x}_{\perp, \ell}) D_0^\alpha(w_{jm}, \mathbf{x}_{\perp, m}) \exp[\alpha\gamma(w_{i\ell}, \mathbf{x}_{\perp, \ell}) + \alpha\gamma(w_{jm}, \mathbf{x}_{\perp, m})]. \quad (\text{D8})$$

Appendix D2 Implementation of the inverse method with peculiar velocities

Appendix D2.1 Strong prior: peculiar velocity equals most likely velocity

Restricting ourselves to a unique LOS, our model reads

$$g_{i\ell}(\gamma) = A(\bar{z})c_1 \int_{-\infty}^{+\infty} \{D_0(x) \exp[\gamma(x)]\}^{\alpha-\beta} \exp \left[-c_2 \frac{[w_{i\ell} - x - v_p(x)]^2}{\{D_0(x) \exp[\gamma(x)]\}^{2\beta}} \right] dx, \quad (\text{D9})$$

where the peculiar velocity, $v_p(x)$, equals the most likely velocity

$$\langle v_p(x) \rangle = \int K^{(v)}(x, y) \gamma(y) dy. \quad (\text{D10})$$

The matrix of partial functional derivatives, \mathbf{G}_i is defined by its contraction over a given field, η , as:

$$(\mathbf{G})_i \cdot \eta \equiv \int G_i(x) \eta(x) dx = \int \mathcal{A}_i(x) \eta(x) dx + \int \mathcal{D}_i(x) \left[\int K^{(v)}(x, y) \eta(y) dy \right] dx, \quad (\text{D11})$$

with

$$\mathcal{A}_i(x) = A(\bar{z})c_1 D_0^{\alpha-\beta}(x) \exp[(\alpha - \beta)\gamma(x)] \{ \alpha - \beta + 2\beta c_2 D_0^{-2\beta} \exp[-2\beta\gamma(x)] [w_i - x - v_p(x)] \} E_i(x), \quad (\text{D12})$$

$$\mathcal{D}_i(x) = A(\bar{z})c_1 D_0^{(\alpha-3\beta)}(x) \exp[(\alpha - 3\beta)\gamma(x)] 2c_2 [w_i - x - v_p(x)] E_i(x), \quad (\text{D13})$$

$$E_i(x) = \exp \left\{ -c_2 \frac{[w_i - x - v_p(x)]^2}{D_0^{2\beta}(x) \exp[2\beta\gamma(x)]} \right\}. \quad (\text{D14})$$

The double integration in the last term of equation (D11) arises because g is effectively a double convolution.

Appendix D2.2 Weak prior: floating peculiar velocity

We aim to determine directly the density and the velocity, while assuming the correlations between these two quantities are known. The model is identical to equation (D9), but the peculiar velocity does not obey equation (D10). The matrix of partial functional derivatives is $\mathbf{G} = (\partial g / \partial \gamma, \partial g / \partial v_p)$. The first component of \mathbf{G} is given by equation (D2). The kernel of the second component is computed as follows:

$$\frac{\partial g}{\partial v_p} = A(\bar{z})c_1 D_0^{\alpha-3\beta}(x) \exp [(\alpha - 3\beta)\gamma(x)] 2c_2 [w_i - x - v_p(x)] E_i(x) \equiv \mathcal{E}_i(x), \quad (\text{D15})$$

where $E_i(x)$ is given by equation (D14). The matrix $\mathbf{G} \cdot \mathbf{C}_0 \cdot \mathbf{G}^\perp$ (where MC_0 is given by equation (35)) is computed as follows:

$$\iint [\mathcal{A}_i(x)\mathcal{A}_j(y)C_{\gamma\gamma}(x, y) + \mathcal{A}_i(x)\mathcal{E}_j(y)C_{\gamma v}(x, y) + \mathcal{E}_i(x)\mathcal{A}_j(y)C_{v\gamma}(x, y) + \mathcal{E}_i(x)\mathcal{E}_j(y)C_{vv}(x, y)] dx dy. \quad (\text{D16})$$

Note that this is a double integral to be compared to the quadruple integral involved in the computation of the equivalent term in the strong prior method (where contraction already involves a double convolution).

This paper has been typeset from a $\text{\TeX}/\text{\LaTeX}$ file prepared by the author.